Ultrafast Charge Transfer and Recombination Dynamics in Monolayer-Multilayer WSe_2 Junctions Revealed by Time-Resolved Photoemission Electron Microscopy

Ce Xu,[1] *Natalie Barden,*[1] *Evgeny M. Alexeev,*[2] *Xiaoli Wang,*[3] *Run Long,*[3] *Alisson R. Cadore,*[2] *Ioannis Paradisanos,*[2] *Anna K. Ott,*[2] *Giancarlo Soavi,*[2,4] *Sefaattin Tongay,*[5] *Giulio Cerullo,*[6,7] *Andrea C. Ferrari,*[2,*] *Oleg V. Prezhdo,*[8,*] *and Zhi-Heng Loh*[1,*]

[1] School of Chemistry, Chemical Engineering and Biotechnology, and School of Physical and Mathematical Sciences, Nanyang Technological University, Singapore 637371, Singapore

[2] Cambridge Graphene Centre, University of Cambridge, Cambridge CB3 0FA, UK

[3] College of Chemistry, Key Laboratory of Theoretical and Computational Photochemistry, Beijing Normal University, Beijing 100875, People's Republic of China

[4] Institute of Solid State Physics, Friedrich Schiller University Jena, Max-Wien-Platz 1, 07743, Jena, Germany

[5] School for Engineering of Matter, Transport and Energy, Arizona State University, Tempe, Arizona 85287, United States

[6] Department of Physics, Politecnico di Milano, Piazza Leonardo da Vinci 32, I-20133 Milano, Italy

[7] IFN-CNR, Piazza Leonardo da Vinci 32, I-20133, Milano, Italy

[8] Department of Chemistry, University of Southern California, Los Angeles, California 90089, United States

[*] Corresponding authors e-mail: acf26@cam.ac.uk (A.C.F.), prezhdo@usc.edu (O.V.P.), zhiheng@ntu.edu.sg (Z.-H.L.)

Abstract

The ultrafast carrier dynamics of junctions between two chemically identical, but electronically distinct, transition metal dichalcogenides (TMDs) remains largely unknown. Here, we employ time-resolved photoemission electron microscopy (TR-PEEM) to probe the ultrafast carrier dynamics of a monolayer-to-multilayer (1L-ML) WSe_2 junction. The TR-PEEM signals recorded for the individual components of the junction reveal the sub-ps carrier cooling dynamics of 1L- and 7L-WSe_2, as well as few-ps exciton-exciton annihilation occurring on 1L-WSe_2. We observe ultrafast interfacial hole (h) transfer from 1L to 7L-WSe_2 on a ~0.2-ps timescale. The resultant excess h density in 7L-WSe_2 decays by carrier recombination across the junction interface on a ~100-ps timescale. Reminiscent of the behavior at a depletion region, the TR-PEEM image reveals the h density accumulation on the 7L-WSe_2 interface, with a decay length~0.60 ± 0.17 μm. These charge transfer and recombination dynamics are in agreement with *ab Initio* molecular dynamics. The computed orbital densities reveal that charge transfer occurs from the basal plane, which extends over both 1L and ML regions, to the upper plane localized on the ML region. This mode of charge transfer is distinctive to chemically homogeneous junctions of layered materials and constitutes an additional carrier deactivation pathway that should be considered in studies of 1L-TMDs found alongside their ML, a common occurrence in exfoliated samples.

Keywords: transition metal dichalcogenides, lateral junction, interfacial charge transfer, time-resolved photoemission electron microscopy, ultrafast spectroscopy, nonadiabatic ab initio molecular dynamics

Layered materials (LMs) are at the center of an ever-expanding research effort.[1-7] Numerous electronic[1-5] and optoelectronic[1,3,6,7] properties have been uncovered in semiconducting transition metal dichalcogenides (TMDs), such as layer-sensitive electronic structures,[8-10] high carrier mobilities ($\sim 10^1 - 10^3$ $cm^2 \cdot V \cdot s^{-1}$),[11-13] superconductivity,[14,15] large exciton binding energies (hundreds meV)[16-19], nonlinear optical response [$\chi^{(2)} \sim 10^{-12}$ $m \cdot V^{-1}$, $\chi^{(3)} \sim 10^{-17} - 10^{-19}$ $m^2 \cdot V^{-2}$],[20-24] and optical properties dominated by excitonic transitions.[16-19,25-29] Along with the ability to fabricate TMDs on wafer-scale,[30-32] these allow the realization of ultrathin nanoelectronic[5] and optoelectronic devices,[6] with with diverse applications, such as transistors,[11-13] photodetectors,[7,33-35] and electroluminescent devices.[36-39]

Layered materials heterostructures (LMHs) comprising two chemically distinct TMDs juxtaposed either vertically or laterally have also been prepared.[31,40] Extensive experimental[41-44] and theoretical[45] studies revealed photoresponse[7,46] and photovoltaic response,[47,48] high ($>10^5$) field-effect ON/OFF ratio,[49] and rectification,[50] as well as intra- and interlayer excitonic physics.[51-55] The behavior of carriers at heterojunctions is dictated by the band alignment of the two TMD components.[56-58] In the case of type-I band alignment, with valence band maximum (VBM) and conduction band minimum (CBM) in the same layer,[59] both electrons (e) and holes (h) transfer to the same TMD, thereby supporting applications that require radiative recombination, such as light-emitting diodes.[38] In the case of type-II band alignment, with VBM and CBM in different layers,[53] photocarriers undergo charge separation and transfer across these heterojunctions, giving rise to applications in photodetectors[7] and photovoltaics.[57,60] Investigations of type-II vertical LMHs by pump-probe spectroscopy revealed interlayer charge transfer within ~50 fs.[61-67] Time-domain density functional theory and nonadiabatic molecular dynamics simulations suggest that the ultrafast interlayer charge transfer is facilitated by quantum coherence and e delocalization.[68]

Electronic structure calculations reveal strong interlayer coupling at the Γ valley of the valence band (VB) and the Q valley of the conduction band (CB), suggesting that these mediate interlayer charge transfer.[69] For lateral LMHs, exciton transfer across a type-I 1L-MoS_2–1L-$MoSe_2$ heterojunction with a velocity[70]~10^4 $m \cdot s^{-1}$ and sub-ps e transfer across a type-II composition-graded 1L-WS_2–1L-WSe_2 interface were reported.[71]

TMD junctions are a complement to LMHs.[72-76] Unlike LMHs, a LM junction (LMJ) comprises the same material at the interface. However, the opposite sides of the interface exhibit distinct bandgaps[73-75], tunable by varying phase,[77] doping,[78] substrate,[79] and number of layers, N.[72,75,76,80,81] We refer to the LMJ between a single-layer (1L) and a multilayer (ML) LM as 1L–ML-LMJ. This can often be found in samples prepared by micro-mechanical cleavage (MC) of bulk (B)-TMDs, in which different regions correspond to different N.[72-74,80] The 1L region of a 1L–ML-LMJ composed of TMDs has a direct bandgap,[82,83] whereas an indirect bandgap is present in the ML region.[82,83] In the case of WSe_2, experimental[80,81] and theoretical[75] studies found that juxtaposing 1L-WSe_2, which has a direct bandgap~1.64 eV,[84] with ML-WSe_2, whose indirect bandgap evolves from 1.51 eV ($N = 2$) to 1.45 eV ($N \geq 4$),[84] yields an interface with a type-I band alignment.[75,80,81] Measurements on a 1L–3L-MoS_2 LMJ by scanning photocurrent microscopy suggested type-II band alignment,[72] whereas Kelvin probe force microscopy on a 1L–14L-MoS_2 LMJ pointed to type-I band alignment.[85]

Compared to the extensive ultrafast spectroscopy studies performed to date on TMD LMHs,[61-67,70,71] the ultrafast dynamics of 1L-ML-LMJs is, to the best of our knowledge, hitherto unexplored, mainly due to the need to combine sub-100-fs temporal- and sub-100-nm spatial resolution to study the dynamics at the interface. The typical μm-scale sizes of MC-TMDs[86] implies similar dimensions for 1L-ML-LMJs, therefore the need for an ultrafast spectroscopy

technique that can simultaneously allow μm to sub-μm resolution. Time-resolved photoemission electron microscopy (TR-PEEM) is complementary to ultrafast optical microscopy[87-89] for investigating spatially resolved ultrafast phenomena. It can resolve the dynamics of trap states in B-semiconductors[71] and perovskite thin films,[90,91] image e motion in B-semiconductors[92] and LMHs,[93] and reveal spatially heterogeneous ultrafast dynamics of TMDs.[94,95]

Here, we use TR-PEEM to investigate the ultrafast e and h dynamics of a 1L–7L WSe_2 type-I LMJ. In addition to sub-ps carrier relaxation dynamics within the individual components, we observe a ~0.2-ps h transfer, followed by ~100-ps charge recombination, across the LMJ. We use nonadiabatic *ab Initio* molecular dynamics to calculate the time constants for h transfer and charge recombination, in agreement with experiments. Analysis of the PEEM images reveals the width of the depletion region at the 1L–7L-WSe_2 interface.

Results and Discussion

The LMJ is prepared as follows. B-WSe_2 crystals are grown by the flux zone method.[16] These are exfoliated by MC on Nitto Denko tape,[86] then again on a polydimethylsiloxane (PDMS)[96] stamp placed on a glass slide for inspection under an optical microscope. Optical contrast[97] is optimized to identify 1L and 1L–7L-WSe_2 prior to transfer. The samples are then placed on 90-nm-SiO_2/Si at 40 °C using *xyz* micro-manipulators under an optical microscope, before increasing the temperature to 60 °C, so that they detach from PDMS and adhere preferably to SiO_2.[96]

Figure 1a reveals regions of different N within the same flake. To characterize and identify N, we perform Raman spectroscopy and atomic force microscopy (AFM). Raman measurements are done with a Horiba LabRam Evolution system equipped with 1800 l/mm grating and volume Bragg filters with a cut-off frequency$\sim$5 cm^{-1} at 532 nm, with a 100× objective (numerical aperture,

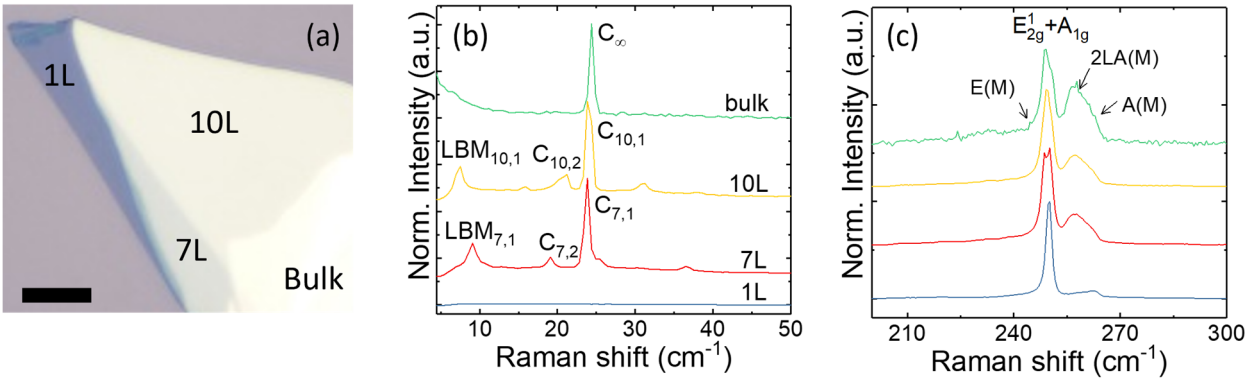

Figure 1. (a) Optical image of 1L-ML-WSe_2. Scale bar: 10μm. (b) Low-frequency and (c) high-frequency Raman spectra as a function of N at 532 nm excitation.

NA=0.9), resulting in a spot size~1μm. AFM measurements are performed with a Bruker Dimension Icon in tapping mode.

Figure 1b plots the low-frequency (<50 cm^{-1}) Raman spectra of the different regions of a WSe_2 flake, and of B-WSe_2. The Raman modes in this frequency range originate from relative motion of the layers and consequently are absent in 1L-WSe_2.[98-102] The shear modes (C) are due to the relative motions of the planes perpendicular to their normal,[98-102] while the layer breathing modes (LBM) are parallel to the normal.[98-102]

The position of the highest frequency C peak, $\mathrm{Pos}(\mathrm{C}_{N,1})$, can be used to derive N as:[15,99]

$$N = \frac{\pi}{2\cos^{-1}\left[\mathrm{Pos}(\mathrm{C}_{N,1})/\mathrm{Pos}(\mathrm{C})_{\infty}\right]}, \quad (1)$$

where $\mathrm{Pos}(\mathrm{C})_{\infty}$ corresponds to B-WSe_2. Figure 1b gives $\mathrm{Pos}(\mathrm{C})_{\infty} \sim 24.4 \pm 0.06$ cm^{-1}. The orange spectrum in Fig.1b has $\mathrm{Pos}(C_{N,1}) \sim 24.0 \pm 0.06$ cm^{-1}. From Eq. 1 we get $N \sim 10 \pm 1$. The red spectrum in Fig.1b has $\mathrm{Pos}(C_{N,1}) \sim 23.8 \pm 0.06$ cm^{-1}, thus $N \sim 7$. Fig.1b for $N = 7$ also shows one LBM at $\mathrm{Pos}(\mathrm{LBM}_{7,1}) \sim 9.1 \pm 0.06$ cm^{-1} and an additional $\mathrm{Pos}(C_{7,2}) \sim 19.1 \pm 0.06$ cm^{-1}, while for 10L-WSe_2 we have $\mathrm{Pos}(\mathrm{LBM}_{10,1}) \sim 7.5 \pm 0.06$ cm^{-1} and $\mathrm{Pos}(C_{10,2}) \sim 21.2 \pm 0.06$ cm^{-1}. In Methods we report a detailed discussion of the spectral fitting accuracy and its influence on N.

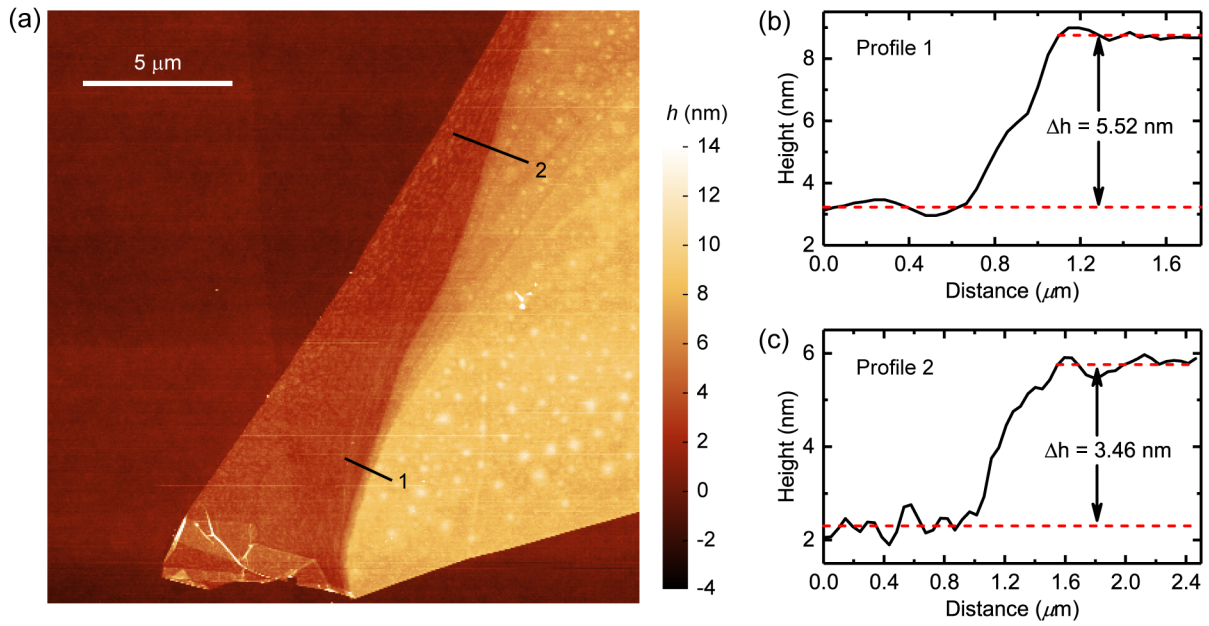

Figure 2. (a) AFM image of 1L-ML-WSe_2 LMJ. (b,c) Height profiles along (b) line 1 and (c) line 2 taken across the LMJ.

Fig.1c plots the high-frequency (200 – 300 cm^{-1}) Raman spectra. For 1L-WSe_2, a single peak is observed ~250 cm^{-1}, associated with the two degenerate, first-order A and E Raman modes.[28,103-107] In B-WSe_2, the spectra show a split for the E^1_{2g} and A_{1g} modes due to a red (blue) shift in the E^1_{2g} (A_{1g}) mode with increasing N.[104-106] The broad peak~260 cm^{-1} can be deconvolved into 2LA(M) and A(M) bands.[105,107] The 2LA(M) mode at ~262 cm^{-1} corresponds to the overtone of the LA phonon branch at the M point of the Brillouin zone (BZ),[105,107] whereas the A(M) mode~258 cm^{-1} corresponds to A-symmetry optical branch at the M point of the BZ.[105,107] The E(M) mode~242 cm^{-1} creates an asymmetry in the lower energy shoulder of E^1_{2g}+A_{1g}.[105,107] This mode red shifts with increasing N.[104-106]

Fig.2a is an AFM image of the 1L-ML-WSe_2 LMJ. The line profiles taken in two different parts of the LMJ (Figs.2b,c) show that the ML regions are predominantly $N \sim 10$ (profile 1) and $N \sim 7$ (profile 2), consistent with the Raman estimate, separated from the ~1L region by a sub-μm-wide $N \sim 6$ strip. For the estimation of N, we consider a 1L-WSe_2 thickness~0.6nm.[31] As the peak

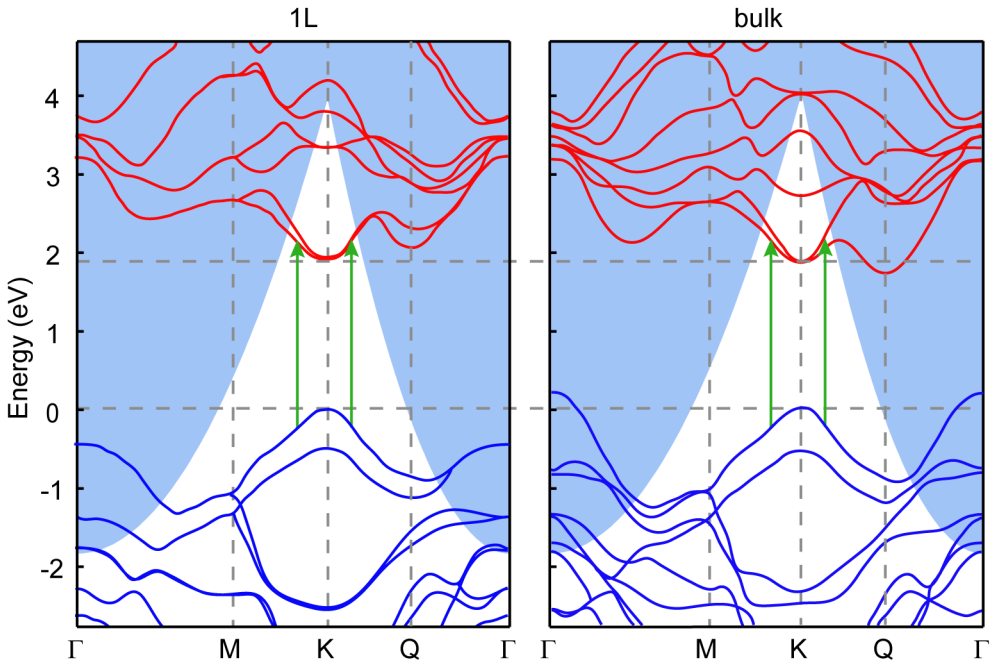

Figure 3. Band structures of 1L- and bulk B-WSe_2 from Ref.108. B-WSe_2 serves as a model for the 6–10L-WSe_2 regions. The 1L–7L WSe_2 LMJ has type-I band alignment, with CBM and VBM residing on 7L-WSe_2. The blue regions are the two-photon probe windows, as required by in-plane momentum conservation, within which photoemission occurs.

positions of the indirect band gap transitions in the photoluminescence (PL) spectrum of ML-WSe_2 remain unchanged within ~1 meV for $N \gtrsim 5$,[8,84] we do not differentiate the 6,7,10L regions in our subsequent analysis, and we refer to these collectively as 6–10L.

Our TR-PEEM setup employs 2.41-eV (515-nm) pump and 3.61-eV (343-nm) probe pulses, with an instrumental response function (IRF) full width at half maximum (FWHM)~55fs. The fluences of the pump and probe pulses are 14 and 1 $\mu J \cdot cm^{-2}$, respectively. Fluence-dependent measurements indicate that pump and probe interactions with the sample involve one and two photons, respectively (see Supporting Information). According to the band structures of 1L- and B-WSe_2 (Fig.3),[108] the latter being a model for 6–10L-WSe_2, photoexcitation at 2.41 eV is a one-photon process at the K valley. Due to the need to conserve lateral momentum in photoemission, the K valleys of 1L- and B-WSe_2 lie beyond the two-photon UV probe window. The probe

windows in Fig.3 are calculated based on ionization potentials of 5.38 and 4.98 eV for 1L- and B-WSe_2, respectively.[109] Therefore, the dynamics of the K valley does not contribute to the PEEM signal. Instead, this originates from Q valleys,[94] which reside within the probe window. Following above band-gap photoexcitation of 1L-WSe_2 near the K valley, e scatter to the Q valley by carrier thermalization. This process, previously shown to occur on the ~10-fs timescale in TMDs,[110] takes place within our IRF FWHM, and leads to the initial population of the conduction band Q valley. The build-up of e population in the Q valley ceases after carrier thermalization is completed on the ~10-fs timescale.[110] As a result of the well-defined probe window (Fig.3) and the restricted regions in the first BZ to which carriers can flow following photoexcitation, energy and/or momentum filtering are not required and not critical for the interpretation of the observed dynamics. The use of two-photon UV probing[94,111] yields dynamics in regions of k space otherwise inaccessible via a one-photon probe.[112]

The interaction with the UV probe at 3.61 eV must be a two-photon process, since one-photon probing does not access the region of the conduction band within which the photoexcited e resides (see Supporting Information). The Q valley lies within the probe window, and can be populated within the width of the IRF by intervalley scattering on a~10fs timescale,[110] as explained in the Supporting Information. For 7L-WSe_2, the VBM at the Γ point also lies within the probe window and can therefore contribute to the PEEM signal.

The sub-80-nm spatial resolution of our TR-PEEM[94,95] is well-suited for resolving the carrier dynamics of 1–7L-WSe_2 LMJ. The TR-PEEM image acquired at 0 fs time delay (Fig.4a) shows that the signal for 1L-WSe_2 is ~50% larger than 7L-WSe_2. This is consistent with the previously reported non-monotonic change in the PEEM intensity as a function of layer number, N, attributed to abrupt changes in the UV photoionization cross-section with N.[113] To investigate the ultrafast

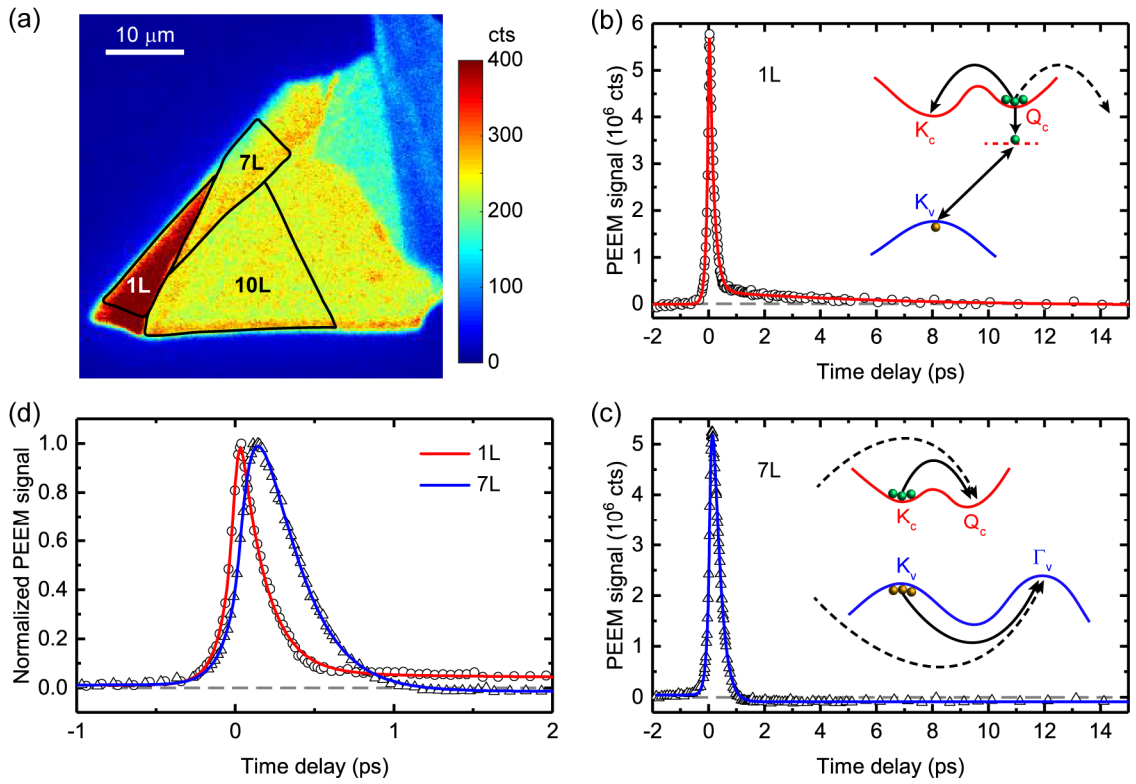

Figure 4. (a) PEEM image of 1L-ML-WSe_2 at 0 fs time delay. (b) Spatially integrated time-dependent PEEM signal from 1L-WSe_2. The inset shows e cooling, dark exciton formation and subsequent exciton-exciton annihilation within 1L-WSe_2, which leads to the bi-exponential decay. Interfacial e transfer to ML-WSe_2 (dashed line) is energetically possible, but not observed. (c) Spatially integrated time-dependent PEEM signal from 7L-WSe_2. The inset shows pathways for e and h cooling within 7L-WSe_2, as well as interfacial charge transfer from 1L-WSe_2 (dashed lines). The exponential rise and decay of the PEEM signal are assigned to e cooling and interfacial h transfer, respectively. (d) Magnified view of normalized time traces of 1L- and 7L-WSe_2 regions at short (<2 ps) time delays. At negative time delays the UV probe arrives at the sample before the pump. The grey dashed line in (b–d) mark the zero baseline.

dynamics of the LMJ, we measure spatially integrated time-dependent PEEM from 1L-WSe_2 (Fig.4b) and 7L-WSe_2 (Fig.4c), with pump and probe fluences of 14 and 1 $\mu J \cdot cm^{-2}$, respectively.

TR-PEEM of 1L-WSe_2 exhibits a bi-exponential decay, with time constants $\tau_1^{1L} = 0.16 \pm 0.01$ ps and $\tau_2^{1L} = 5.13 \pm 0.97$ ps, and an amplitude ratio $A_1^{1L}/A_2^{1L} = 24.9 \pm 2.4$. For 7L-$WSe_2$, TR-

PEEM shows a delayed rise followed by a decay, with $\tau_r^{7L} = 0.11 \pm 0.01$ ps and $\tau_d^{7L} = 0.22 \pm 0.01$ ps, respectively (Fig.4d). The decay is followed by a weak, long-lived negative offset, due to the generation of excess h in 7L-WSe_2. The peak of the 1L-WSe_2 signal (Fig.4d) is delayed~31fs relative to time-zero. However, this does not reflect the finite time for intervalley e scattering from K to Q valley, estimated to occur with a time constant of 16 ± 5 fs.[114] Instead, it arises from the finite IRF FHWM~54fs, obtained from the global fit. This is consistent with Ref.115, which showed that K and Q valleys are simultaneously populated by above-band-gap, 2.48-eV photoexcitation.[115] Our ~50-fs time resolution does not allow the timescale for K to Q intervalley scattering to be precisely determined, since it occurs within our temporal resolution. On the other hand, the delay in the peak of the 7L-WSe_2 signal can be ascribed to the ~0.1-ps K to Q intervalley e scattering (see below).

Following our previous TR-PEEM investigation of CVD-grown 1L-WSe_2,[94] we assign τ_1^{1L} to depopulation of the Q valley, based on intervalley scattering to the K valley being energetically favorable (Fig.3), and τ_2^{1L} to exciton-exciton annihilation, based on the observed acceleration of the annihilation process with higher excitation density.[116,117] Note that the PEEM signal does not decay completely on the sub-ps timescale. At 500-fs time delay, it is still ~10% of the peak signal. Hence, after initial e cooling on the timescale of τ_1^{1L}, there exists a small, but non-negligible, residual population in the Q valley, suggestive of dark exciton formation.[115,118] The observed dynamics differ from previous works that employed resonant excitation of the A exciton transition,[114,115] which reveal exciton dynamics that evolve on the ps timescale.[114,115] Our experiments employ above-band-gap excitation at 2.41 eV, where free carriers dominate the initial ultrafast dynamics. We now consider the various possible pathways by which e can leave the conduction band Q valley of 1L-WSe_2; control experiments performed on an isolated 1L-WSe_2

flake (see below) are then used to eliminate some of these pathways. First, since the K valley is lower than the Q valley in the conduction band of 1L-WSe_2,[108,119,120] carrier cooling via intervalley scattering[28] leads to the transfer of e population from the Q valley to the K valley. Second, Q valley e can transfer across the LMJ interface to the lower-lying Q valley of 7L-WSe_2. Third, they can form dark excitons,[115,118] comprising Q valley e and K valley h (VBM), where e and h have different momenta, therefore cannot undergo radiative recombination. The observed ~0.3-ps delay, assigned to indirect exciton formation following above-band-gap excitation of 1L-WSe_2,[115] is consistent with our τ_1^{1L}. These dark excitons, which reside in the probe window and have non-vanishing momenta, can subsequently undergo exciton-exciton annihilation,[118] thereby resulting in the observed few-ps decay. A similar Auger-mediated annihilation dynamics of dark excitons in 1L-WSe_2 was identified by time-resolved mid-infrared (~6–9 μm) probing of intra-excitonic transitions.[118] Global fitting of the time traces at different excitation fluences (11 – 21 $\mu J \cdot cm^{-2}$) yields an annihilation rate constant $\gamma = 0.46 \pm 0.02$ $cm^2 \cdot s^{-1}$ (see Supporting Information for details), consistent with $\gamma \sim 0.35$ $cm^2 \cdot s^{-1}$ obtained from a combination of PL spectroscopy and Monte-Carlo simulations of 1L-WSe_2,[121] and with those obtained from time-resolved optical microscopy for 1L-$MoSe_2$ (0.33 ± 0.06 $cm^2 \cdot s^{-1}$)[122] and 1L-WS_2 (0.41 ± 0.02 $cm^2 \cdot s^{-1}$).[116]

To understand the temporal behavior of the TR-PEEM signal for 7L-WSe_2 (Fig.4c), we first note that CBM and VBM of ML-WSe_2, located at the Q and Γ valleys, respectively, both reside within the probe window (Fig.3). The Q valley is located 150 meV below the K valley in the CB, while the Γ valley lies 180 meV above the K valley in the VB.[108] Photoexcitation of 7L-WSe_2 at 2.41 eV occurs in the vicinity of the K valley, and is followed by carrier cooling, channeling e from K to Q valley (CBM), and h from K to Γ (VBM). Since the acquisition of TR-PEEM images involves referencing to the PEEM image collected with long (250 ps) temporal separation of the

pump and probe pulses (see Methods), the appearance of e (h) in the probe window leads to a rise (decay) of the TR-PEEM signal. The 7L-WSe_2 signal also indicates charge transfer across the 1L–7L-WSe_2 interface. Since CBM and VBM of 7L-WSe_2 both reside in the probe window, e (h) transfer would result in the appearance of excess e (h) in 7L-WSe_2, in turn giving rise to a positive (negative) offset in the TR-PEEM signal. Fig.4c shows a negative baseline offset at time delays >1 ps, suggesting the presence of sub-ps h transfer across the LMJ. According to scanning tunneling spectroscopy, the VB offset between 1L- and 2L-WSe_2 is 0.12 eV,[80] thus making h transfer from 1L- to ML-WSe_2 energetically favorable. As such, we assign the $\tau_d^{7L} \sim 0.22$ ps component to h transfer. On the other hand, we attribute $\tau_r^{7L} \sim 0.11$ ps to e cooling via K → Q intervalley scattering, slower than that for 1L-WSe_2. We note that Ref.123 analyzed the temperature-dependent optical reflectance of 1L- and 2L-WS_2 to extract their homogeneous linewidths. Their results suggest enhanced exciton-phonon scattering in 2L-WS_2 compared to 1L-WS_2. However, homogeneous linewidths give optical dephasing times,[124] and do not directly probe the intervalley scattering timescales.[125] A more direct comparison of K to Q intervalley scattering times can be obtained from time- and angle-resolved photoemission spectroscopy measurements of 1L-WSe_2[115] and B-WSe_2.[126] While photoexcitation of 1L-WSe_2 does not reveal any noticeable delay between the population of the K and Q valleys,[115] photoexcitation of B-WSe_2 yields a delayed appearance of the Q valley, with its population peaking ~0.2 ps after photoexcitation, from which an intervalley scattering timescale ~70 ± 15 fs was inferred.[126] These results are consistent with ours, which suggest a more rapid K to Q intervalley scattering for 1L-WSe_2 than 7L-WSe_2. The few-ps decay observed in 1L-WSe_2, assigned to exciton-exciton annihilation,[94] is absent because the small exciton binding energies of B-TMDs, typically on the order of 10 meV,[126-128] do not support stable excitons in 7L-WSe_2 at room temperature.

Note that the negative offset in Figs.4c,d, assigned to h transfer, could also potentially be due to matrix elements effects,[129] causing the photoionization cross-section to be larger for the CB Q valley than the VB Γ valley. To verify the occurrence of ultrafast h transfer and to elucidate possible ultrafast e- and/or exciton transfer across the 1L–7L WSe_2 interface, we perform TR-PEEM on an isolated 1L-WSe_2 flake under identical experimental conditions (see Supporting Information). This cannot exhibit any charge or energy transfer dynamics. Its TR-PEEM time trace, shown in the Supporting Information, can be fit to a bi-exponential decay, with a fast $\tau_1^{1L} = 0.13 \pm 0.01$ ps, a slow $\tau_2^{1L} = 3.28 \pm 0.10$ ps, and $A_1^{1L}/A_2^{1L} = 9.0 \pm 0.4$. As for the 1L-$WSe_2$ in our LMJ, the fast and slow decays are attributed to e leaving the Q valley and exciton-exciton annihilation, respectively. Global fitting of the slow decay component at different excitation fluences yields $\gamma \sim 0.30 \pm 0.04$ $cm^2 \cdot s^{-1}$ (see Supporting Information). The nearly identical τ_1^{1L} for both isolated 1L-WSe_2 and that in the LMJ rules out e transfer as an additional deactivation pathway for the Q valley e of 1L-WSe_2 in our LMJ. Compared with isolated 1L-WSe_2, the slower exciton population decay τ_2^{1L} of the 1L-WSe_2 in our LMJ excludes the possibility of ultrafast exciton transfer occurring at the 1L–7L-WSe_2 LMJ, which would accelerate the decay of the exciton component of the TR-PEEM signal. Instead, the slower exciton population decay of 1L-WSe_2 in our LMJ is consistent with ultrafast h transfer depleting the initial density of dark excitons, hence decelerating exciton-exciton annihilation.[116] A lower initial exciton density also reduces the relative contribution of exciton-exciton annihilation to the overall PEEM signal, thereby accounting for the larger A_1^{1L}/A_2^{1L} for 1L-WSe_2 in our LMJ. Comparing A_1^{1L}/A_2^{1L} for LMJ and the isolated flake, we find that the initial exciton density in the LMJ is ~40 % that of the isolated flake. A similar reduction in the initial exciton density is obtained when one considers the measured τ_2^{1L} and γ for both samples (see Supporting Information). Our interpretation that the observed negative offset in the 7L region

of 1L-7L-WSe_2 arises from interfacial h transfer is consistent with a previous time-resolved photoemission study of bulk-WSe_2,[126] which did not observe the 0.22-ps decay component that we ascribe to h transfer. Instead, the dynamics reported in Ref. 126 are dominated by a long-lived (tens of ps) population of Q valley electrons. Our control experiment on an isolated 1L-WSe_2 flake (see Supporting Information) proves that e transfer across the 1L–7L-WSe_2 interface does not occur, thus allowing us to attribute any differences in the ps dynamics of excitons to h transfer giving rise to a lower initial exciton density.

The absence of exciton transfer across the interface, despite the type-I band alignment of our 1L–7L WSe_2 LMJ, can be rationalized in terms of the large exciton binding energy (0.37 eV)[130] of 1L-WSe_2, the vanishingly small exciton binding energy of 7L-WSe_2,[127] and the small VB and CB offsets at the 1L–7L-WSe_2 LMJ. These factors make exciton transfer energetically unfavorable. The apparent absence of interfacial e transfer requires further investigation. We note that exciton formation does not explain the absence of e transfer across the LMJ, since h transfer may also be similarly impeded. One possible explanation is that ultrafast K to Q intervalley e scattering within 7L-WSe_2, with $\tau_r^{7L} = 0.11 \pm 0.01$ps, could inhibit e transfer by Pauli blocking. Given that e transfer is mediated by the strong interlayer coupling at the Q valley,[69] it is conceivable that the population of the Q valley of 7L-WSe_2 could inhibit e transfer across the LMJ.

The negative baseline offset that appears in the TR-PEEM time trace of 7L-WSe_2 in our LMJ (Fig.4c) points to the existence of a long-lived h population on 7L-WSe_2. Fig.5a shows the TR-PEEM images for pump-probe time delays >1 ps. Extending the pump-probe time delay to 250 ps shows that the negative offset decays with a time constant~108 ± 9 ps (Fig.5b), signaling the h disappearance from 7L-WSe_2 on this timescale. TR-PEEM is unable to detect carrier recombination within 7L-WSe_2 because both its VBM and CBM are within the probe window.

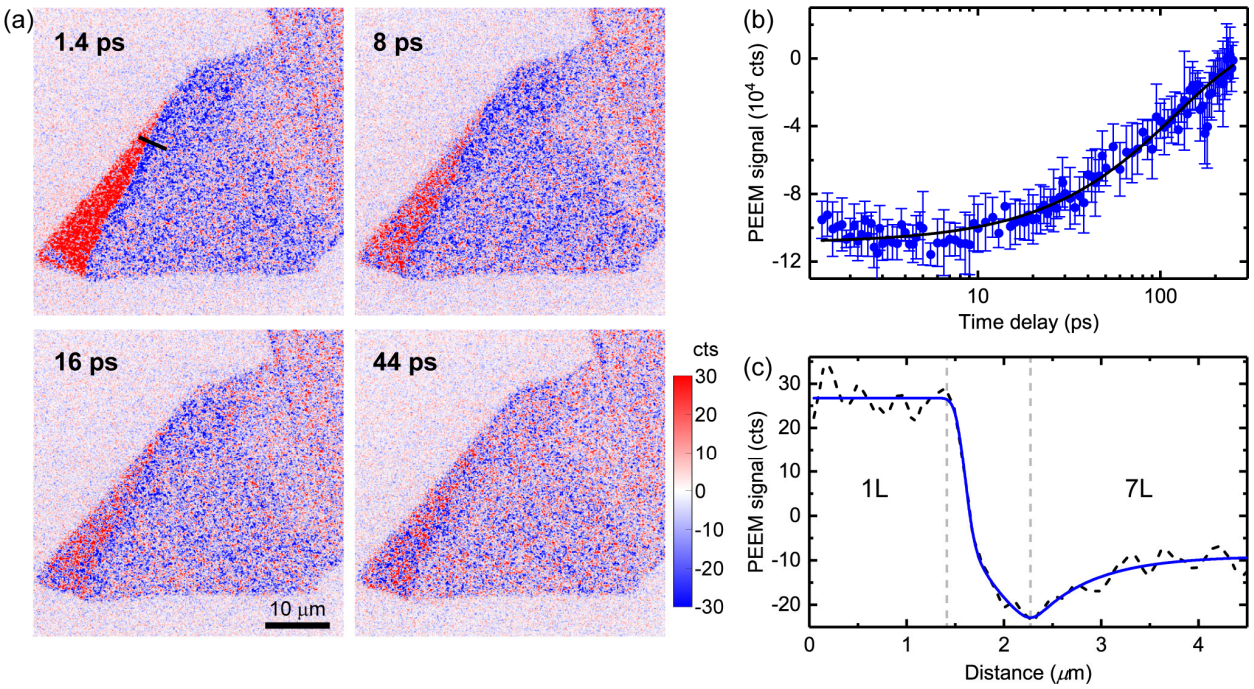

Figure 5. (a) Differential PEEM images with time delays from 1.4 to 44 ps. (b) Time trace of 7L-WSe_2 PEEM with pump-probe time delay up to 250 ps, undergoing an exponential decay. The black line shows the fit to a single exponential decay. (c) PEEM signal profile along the black line on the 1.4-ps image in (a). The PEEM signal changes from positive, in the 1L region, to negative in 7L, and has a rise within the 7L region fitted with an exponential function

The h disappearance from the probe window is thus attributed to carrier recombination across the 1L–7L junction. To the best of our knowledge, the interfacial carrier recombination times for TMD 1L–ML LMJs and lateral TMD LMHs were not previously reported. The ~100-ps recombination time is in the range observed for vertical TMD LMHs.[61,64,131] Inspection of the TR-PEEM images collected for the 7L-WSe_2 region at >1-ps time delays, when carrier cooling no longer contributes to the signal, reveals h accumulation at the 1L–7L-WSe_2 interface (Fig.5a). The higher h density at the interface can also be seen from the lineout of the TR-PEEM signal (Fig.5c), which reveals a decrease in h density with distance from the 1L–7L-WSe_2 interface. This might be assigned to the depletion region that exists at the 1L–7L-WSe_2 interface. Fitting the h density distance dependence (see Supporting Information) suggests a depletion width~0.60±0.17μm,

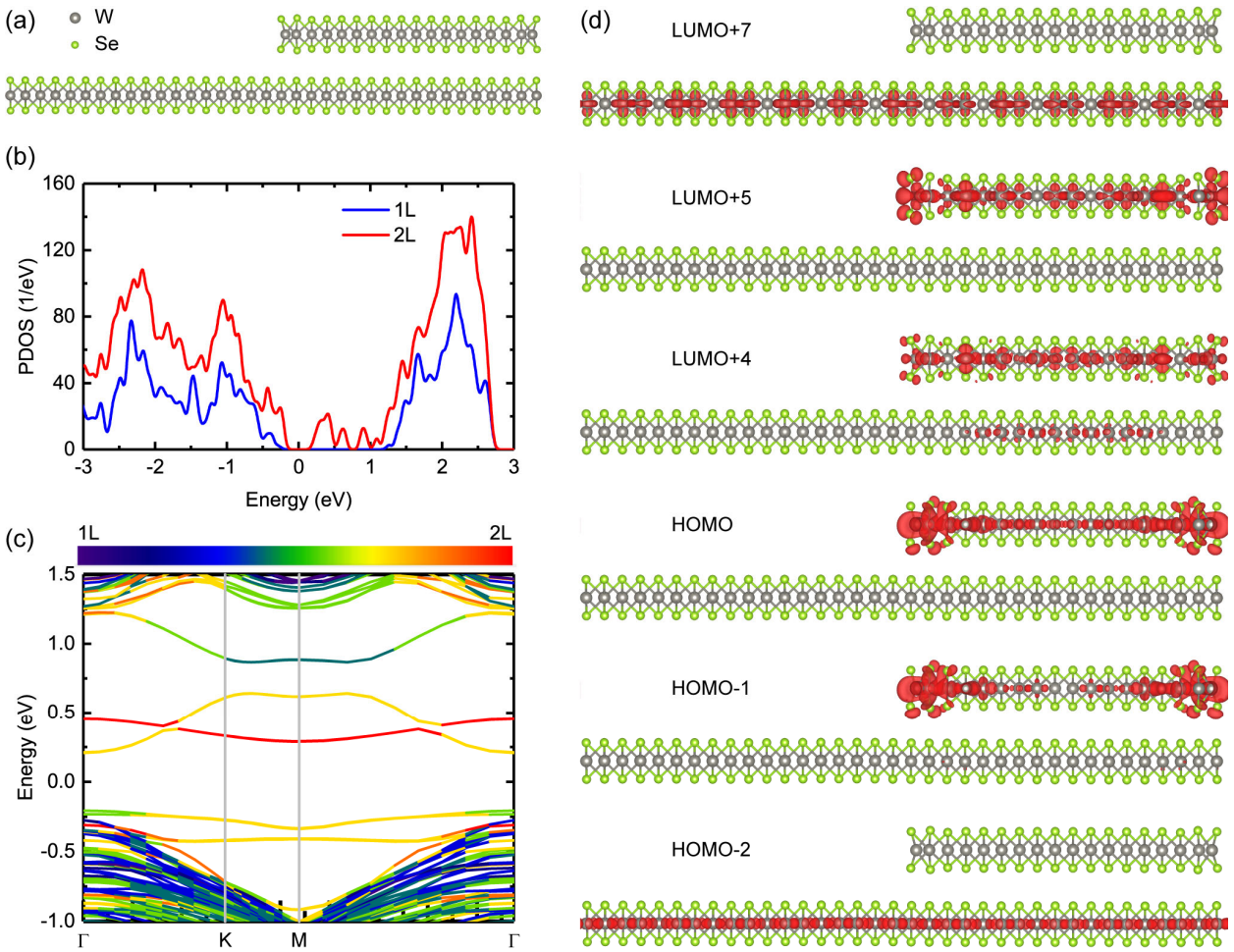

Figure 6. (a) Side view of optimized geometry of 1L–2L-WSe_2 LMJ. (b) Partial density of states and (c) band structure of 1L–2L-WSe_2. The states in the band gap represent edge states. The zero energy corresponds to E_F. The band structure is color coded to show the relative contributions of 1L and 2L regions to the individual bands. (d) Charge densities of the various states involved in the ultrafast dynamics at the 1L–2L-WSe_2 LMJ. The isosurface is set at 0.001 e/Å^3.

similar to the 0.32μm for 1L-WSe_2-1L-MoS_2 LMJ.[132] The existence of a depletion region is consistent with h transfer across the LMJ, since it would not exist without excess carriers.[132]

To get further insights on the ultrafast dynamics of our LMJ, we perform *ab Initio* quantum dynamics on a model 1L–2L-WSe_2 LMJ (Fig.6a, see Supporting Information for details). The 162-atom structure was previously used to study electronic properties of WSe_2 LMJs, exhibiting properties similar to those of structures with a larger N.[75] Including all 7 layers would make the

calculations prohibitively expensive computationally. The bottom 1L-WSe_2 contains 108 atoms periodically replicated in two-dimensions. To create a 2L-WSe_2, a second layer is added on half of the bottom 1L-WSe_2. Geometry optimization gives a Se···Se distance~3.36 Å between the two 1L-WSe_2, in agreement with Ref.75. The calculated density of e states and band structure for the model 1L–2L-WSe_2 LMJ are shown in Figures 6b and 6c, respectively. The charge densities of the key states involved in the excitation dynamics are in Fig.6d. The simulated system can be viewed either as a 108-atom bottom 1L-WSe_2 with a 54-atom top half-layer, or as a 54-atom 1L-WSe_2 on the left and a 108-atom 2L-WSe_2 on the right. Necessarily, the top half-layer contains edges, which create defect states inside the bandgap of 1L-2L-WSe_2. The defect states appear mid-gap (Fig.6b) and can be identified by the flat band dispersion (Fig.6c) as well as by their charge densities (see Supporting Information). Because the size of the top layer is large in experiments, on the order of ~1 μm (Fig.1a), the relative contribution of edges to the overall dynamics is likely insignificant. Therefore, the defect states created by edges are excluded in the simulations.

We simulate h and e dynamics to provide insights into why only interfacial h transfer is observed, without interfacial e transfer, even though both processes are energetically favourable. The simulated h and e dynamics are in Figs.7a,b, respectively. h transfer occurs from the top of the 1L-WSe_2 VB, represented by the HOMO–2 orbital, to the top of the 2L-WSe_2 VB region, represented by the HOMO (Fig.6d). The simulations give a time constant~339 fs for h transfer, in agreement with the measured $\tau_d^{7\mathrm{L}}$ ~ 0.22 ps. The transfer is ultrafast because it occurs though a dense manifold of VB states (Fig.6c). The average absolute nonadiabatic coupling between HOMO–2 and HOMO is 10.5 meV. The simulated time constant for h cooling within 2L-WSe_2 is 904 fs, ~3× longer than the interfacial h transfer time. Hence, h cooling might not be observed experimentally because it is outpaced by interfacial h transfer.

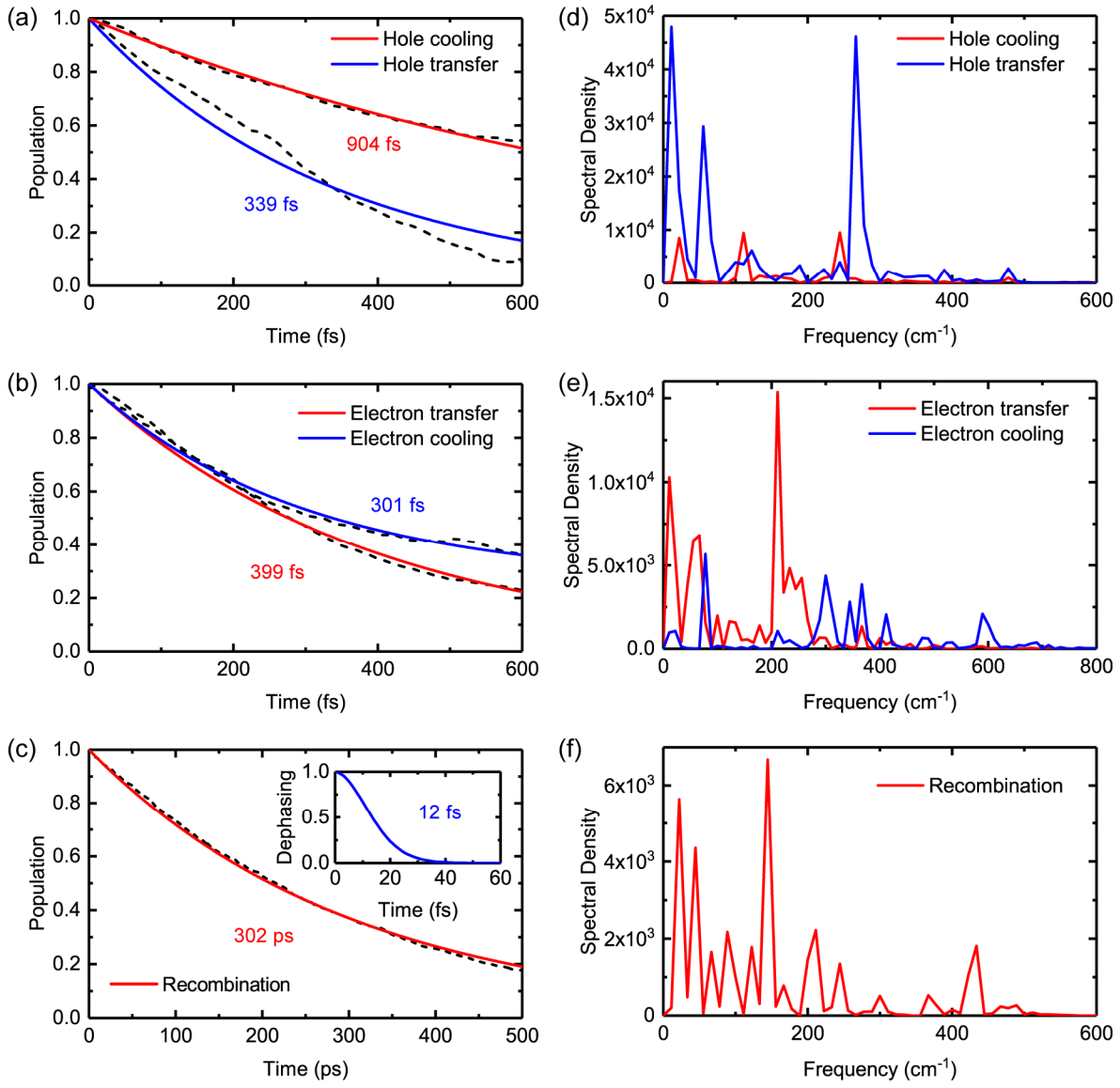

Figure 7. Simulated dynamics for (a) h transfer and cooling, (b) e transfer and cooling, (c) interfacial e-h recombination. Spectral densities characterizing phonon modes involved in the charge dynamics for (d) h transfer and cooling, (e) e transfer and cooling, (f) e-h recombination.

Beyond h transfer, the simulations also elucidate why interfacial e transfer is not observed, despite the type-I band alignment at the 1L–7L-WSe_2 interface. The simulated time constant for e transfer from the CBM of 1L-WSe_2 (LUMO+7 in Fig.6d) to the CBM of 2L-WSe_2 (LUMO+4) is 399 fs (Fig.7b), whereas that for e cooling within 2L-WSe_2 is 301 fs, i.e. ~1.3× faster than e transfer.

Thus, e transfer is suppressed at the expense of e cooling. Given that e transfer is mediated by the strong interlayer coupling at the Q valley,[69] it is conceivable that the population of the Q valley of 7L-WSe_2 by e cooling could inhibit e transfer across the LMJ.

To explain charge recombination being two orders of magnitude slower compared to interfacial h transfer, we model recombination across the 1L–7L-WSe_2 interface by considering the LUMO+7 and HOMO orbitals (Fig.6d), which correspond to the CBM of 1L-WSe_2 and the VBM of 2L-WSe_2, respectively. The simulations give a recombination time~302 ps (Fig.7c), consistent with the experimental~108 ps. Charge recombination is slower than charge transfer for several reasons. First, recombination occurs across a large energy gap (1.31 eV). Second, the nonadiabatic coupling between the orbitals that participate in charge recombination (1.35 meV) is one order of magnitude smaller than between the orbitals that participate in e (12.2 meV) and h (10.5 meV) transfer. Third, recombination involves a rapid 12-fs loss of quantum coherence (Fig.7c, inset), which slows down quantum dynamics. This is exemplified by the quantum Zeno effect,[133] whereby transitions stop completely if one attempts to measure continuously and precisely the quantum state of the system, giving rise to infinitely fast coherence loss.[133]

The simulations also provide insights into the relative importance of carrier cooling vs. carrier transfer for e and h. The frequencies of the phonon modes that accommodate the excess energy lost by the electronic subsystem during these nonradiative processes are in Figs.7d,e for h and e transfer, respectively, and in Fig.7f for e-h recombination. These spectral densities are obtained as Fourier transforms of the phonon-induced fluctuations of the corresponding energy gaps. A higher intensity of a peak at a given frequency and the presence of multiple phonon modes favor stronger nonadiabatic coupling. Fig.7d shows that the intensity of major phonon modes for h transfer is ~5× larger than that for h cooling, leading to stronger nonadiabatic coupling, thus

faster h transfer. The situation changes for e dynamics. Even though the peaks are higher for e transfer than cooling, the difference is less pronounced. In addition, e cooling is promoted by several high frequency modes~300–400 and 600 cm^{-1}, which do not participate in e transfer. As a result, e cooling is faster than e transfer (Fig.7b). The peak~267 cm^{-1}, contributing strongly to the h transfer process, can be assigned to the 2LA(M) mode, observed at~260 cm^{-1} in the Raman spectra (Fig.1c). The frequencies <250 cm^{-1} can be attributed to various transverse and longitudinal acoustic modes, shear modes, and their overtones or combinations. Long-wavelength acoustic modes influence charge wave functions over nanometer scales, facilitating charge transfer.[68,95] Multiple vibrations contribute to the charge dynamics because the interface between 1L and ML regions breaks the symmetry and relaxes electron-phonon coupling selection rules for pristine systems. The electron-vibrational coupling matrix elements, $\langle i|\nabla_r|j\rangle$, for nonradiative charge transfer and recombination are different from the Raman matrix elements,[134] and have weaker selection rules, because optical spectra are determined by operators with high symmetries describing, e.g., linearly polarized light, while the gradients with respect to vibrational motions, ∇_r, represent many different symmetries. This fact rationalizes why more modes participate in the charge dynamics than the Raman spectra.

The salient experimental and theoretical observations are summarized below.

(1) The sub-ps decay constants for the 1L-WSe_2 region of the 1L–7L-WSe_2 LMJ ($\tau_1^{1L} = 0.16 \pm 0.01$ ps) and for an isolated 1L-WSe_2 flake ($\tau_1^{1L} = 0.13 \pm 0.01$ ps) are similar. τ_1^{1L} is assigned to the depopulation of the Q valley in 1L-WSe_2. The similarity of τ_1^{1L} rules out sub-ps electron transfer from the 1L- to the 7L-WSe_2 region of the LMJ, which would accelerate the decay.

(2) The few-ps decay of 1L-WSe_2 is slower for the 1L-7L-WSe_2 LMJ ($\tau_2^{1L} = 5.13 \pm 0.97$ ps) than for the isolated 1L-WSe_2 flake ($\tau_2^{1L} = 3.28 \pm 0.10$ ps). τ_2^{1L} is assigned to exciton-exciton

annihilation in 1L-WSe_2. The slower exciton-exciton annihilation for the LMJ than the isolated flake, according to second-order kinetics,[116,117] is suggestive of the initial exciton density being lower in the LMJ than the isolated flake. Since e do not transfer from 1L- to 7L-WSe_2 in the LMJ, its lower initial exciton density suggests h transfer from 1L- to 7L-WSe_2.

(3) The 7L-WSe_2 region of the LMJ exhibits an ultrafast decay ($\tau_d^{7L} = 0.22 \pm 0.01$ ps) and a long-lived, >100-ps negative offset. This implies h transfer because both CBM and VBM of 7L-WSe_2 reside in the probe window, such that the appearance of excess h in 7L-WSe_2 would yield a lower PEEM signal, resulting in a negative offset, that could also arise from matrix element effects.[129]

(4) Ab initio nonadiabatic molecular dynamics simulations on a 1L–2L-WSe_2 LMJ (used as a model for the experimental 1L–7L-WSe_2 LMJ) reveal that h transfer from 1L- to 2L-WSe_2 is ~3× faster than h cooling within 2L-WSe_2. Hence, we assign the ultrafast decay in the 7L-WSe_2 region to h transfer from 1L-WSe_2 instead of h cooling within 7L-WSe_2.

(5) A section of the PEEM image normal to the 1L–7L-WSe_2 junction reveals a depletion region (Fig.5a). This, and the negative PEEM signal, imply h accumulation in the 7L-WSe_2 region. Note that a depletion region, by definition, requires the presence of excess carriers.[135]

Conclusions

We studied the dynamics of photoexcited carriers at the 1L–7L-WSe_2 interface by using a combination of TR-PEEM and nonadiabatic *ab Initio* molecular dynamics. Since the low-energy, 7.22-eV two-photon photoionization probe provides a well-defined probe window and carriers can only flow to restricted regions of the first Brillouin zone, energy and/or momentum resolution are not required for the interpretation of the experimental results. Instead, interpretation of the observed ultrafast dynamics is based primarily on comparing the ultrafast dynamics of the 1l–7L-

WSe_2 LMJ sample to those of the isolated 1L-WSe_2 flake. The experimental and theoretical results, summarized above, suggest interfacial h transfer from 1L- to 7L-WSe_2 within the LMJ on a ~0.2-ps timescale. The resultant excess h density in 7L-WSe_2 eventually decays by carrier recombination across the 1L–7L-WSe_2 interface on a 100-ps timescale. The experimental timescales for interfacial h transfer and e-h recombination are consistent with *ab Initio* quantum dynamics simulations. These results suggest that ML regions alongside 1L ones can influence the ultrafast carrier dynamics of the latter. As such, analysis of time-resolved data should consider ultrafast charge transfer across the 1L–ML interface as an additional carrier deactivation pathway. Charge transfer does not occur in-plane, unlike lateral LMHs.[70,71] Instead, as the charge density plots in Fig.6d suggest, h transfer involves the shift of h density from the basal plane (HOMO–2), extended over 1L and 2L regions, to the top plane (HOMO), localized on the 2L region. The interfacial charge transfer in 1L–7L-WSe_2 is thus more akin to that occurring in vertical LMHs, albeit with chemically identical bottom and top layers. Such a mode of charge transfer is distinctive to LMJs.

The e transfer dynamics of 1L-$MoSe_2$–1L-$MoSe_2$, 1L-WS_2–1L-WS_2, and 1L-WSe_2–1L-WSe_2, each with an underlying graphene substrate, was previously reported.[136] However, in Ref. [136] the underlying graphene substrate also participates in ultrafast charge transfer.[137] While picosecond interlayer e transfer following above-band-gap photoexcitation was resolved in Ref. [136], the timescale for h transfer to the Γ valley remains elusive. The h dynamics at the Γ valley is of particular interest because the spatial extension of the Γ valley wave functions in the out-of-plane direction allows it to play an important role in mediating interlayer h transfer.[69] Our results yield $\tau_d^{7L} \sim 0.2$ ps for h transfer to the Γ valley of 7L-WSe_2, suggesting that LMJs can also support ultrafast interlayer h transfer.

Methods

Ultra-low frequency Raman spectral fitting accuracy. Raman spectroscopy can determine N in TMDs.[98-102] However, accurate estimation for $N > 3$ requires measurements of $\mathrm{Pos}(C_{N,1})$ with high precision (typical shift ranging from 0.05 to 0.3 cm^{-1} vs. a typical spectral resolution~0.6 cm^{-1}). Peak position evaluation with sub-pixel accuracy can be achieved via spectral fitting. We demonstrate the feasibility of this approach by measuring the changes of $\mathrm{Pos}(C_{N,1})$ in 2–12L-MoS_2 (Fig.8). Regions of different thickness are identified using optical contrast and confirmed by AFM. $\mathrm{Pos}(C_{N,1})$ is in Fig.8b (black circles), showing an increase with N in excellent agreement with Eq.

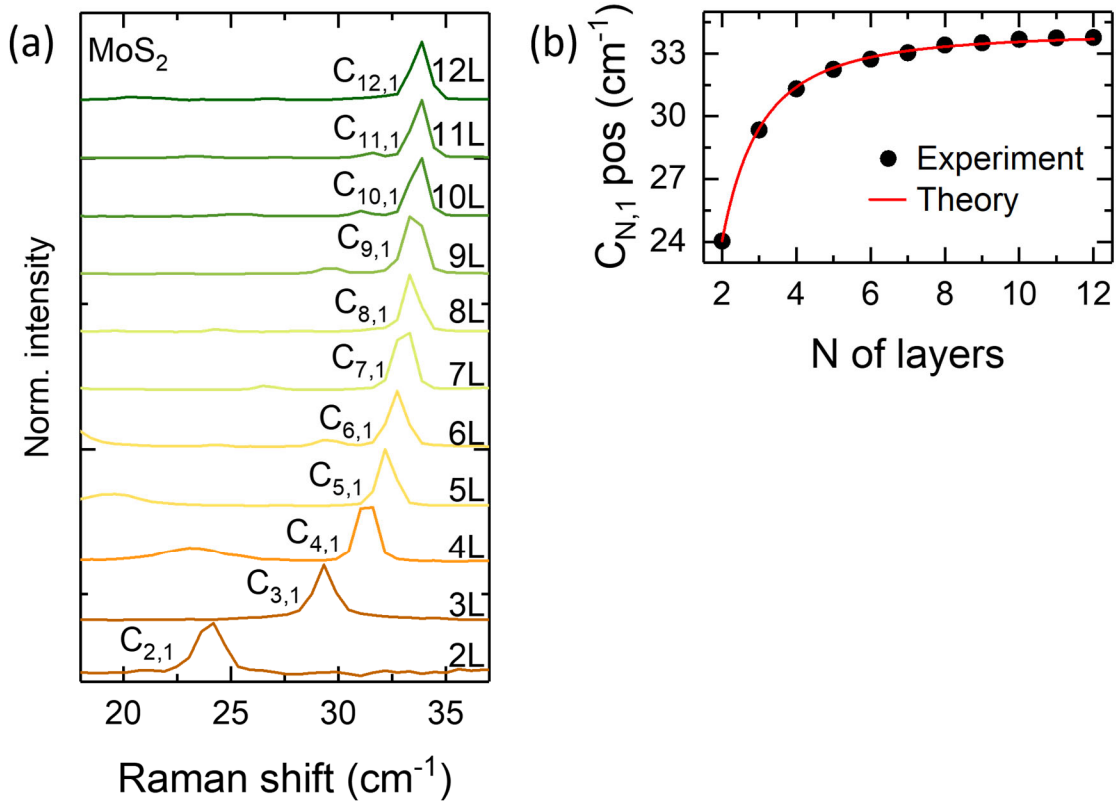

Figure 8. (a) Raman spectra normalized to their maximum intensities showing the $C_{N,1}$ peak in 2-12L-MoS_2. (b) $\mathrm{Pos}(C_{N,1})$ vs. N: experiments (black circles) are in agreement with Eq. 1 (red line).

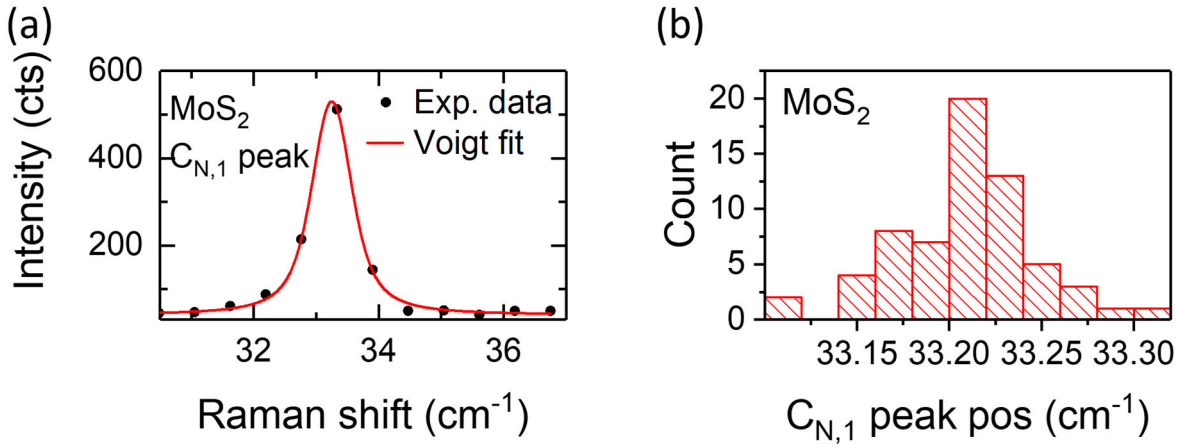

Figure 9. (a) An example Pos($C_{N,1}$) fitting for a $N > 15$ ML-MoS_2 flake. Black dots: experimental data. Red curve: Voigt fit. (b) Histogram showing the variation of Pos($C_{N,1}$) by acquiring spectra at 64 different points.

1, with $\mathrm{Pos}(C)_\infty \sim 33.99$ cm^{-1}. $C_{11,1}$ and $C_{12,1}$ can be resolved in Fig.8a, even though Pos($C_{12,1}$) – Pos($C_{11,1}$) ~ 0.02 cm^{-1}. There are three key factors that contribute an error to Pos($C_{N,1}$): 1) general fitting error, 2) statistical error, and 3) sub-pixel specific fitting error.

First, we evaluate general fitting error. Fig.9a is an example of spectral fitting, with black circles representing experimental data and the red line a Voigt fit. The fitted curve is in a good agreement with experimental data, with coefficient of determination $R^2 \sim 0.99$. The typical Pos$(C_{N,1})$ error is ~ 0.02 cm^{-1} and likely represents the lower boundary.

Second, we look at statistical error, i.e., variations of Pos$(C_{N,1})$ in different areas with the same *N*, which can be caused by changes of material properties (e.g. strain or disorder), as well as random noise on the CCD detector. The latter can have a strong effect on Pos$(C_{N,1})$ due to the small number of data points (5 – 7) used for spectral fitting. To evaluate typical values of statistical error, we acquire spectra in 64 areas within a $N > 15$ ML-MoS_2. Fig.9b is an histogram of fitted Pos$(C_{N,1})$, with a mean~33.2cm^{-1} and standard deviation~0.04cm^{-1}, consistent with other samples.

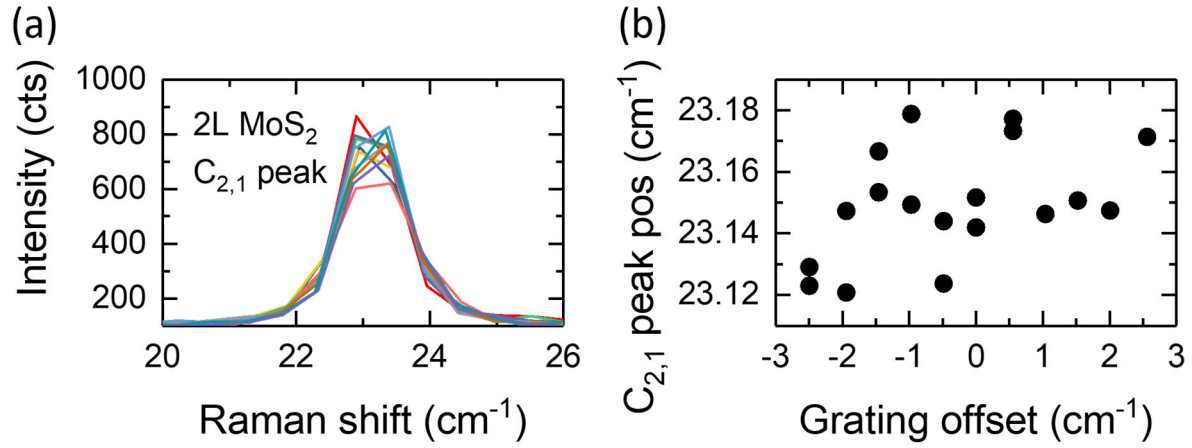

Figure 10. (a) $C_{2,1}$ for different positions of the spectrometer grating. (b) Pos($C_{2,1}$) as a function of relative grating position offset compared to the original one.

Third, we consider the error associated with subpixel fitting. Since FWHM($C_{N,1}$) is comparable with the spectral resolution, the extracted $\mathrm{Pos}(C_{N,1})$ can be very sensitive to pixel registry, i.e., microscopic alignment of the light dispersed by grating and CCD pixel array. To investigate this, we record the variation of $\mathrm{Pos}(C_{N,1})$ with grating angle, projecting the same signal onto different combination of CCD pixels. Fig.10a,b plot Raman spectra and $\mathrm{Pos}(C_{2,1})$, respectively, for 2L-MoS_2 and different grating positions, indicated by the relative offset to the first two measurements. The variation of $\mathrm{Pos}(C_{2,1})$ has standard deviation ~0.02 cm^{-1} and a maximum ~0.06 cm^{-1}. As $C_{N,1}$ peaks in regions with different N will be detected differently, depending on pixel registry, we use the highest of these two numbers to evaluate the fitting error.

We can now evaluate the expected error in WSe_2 thickness identification. Table 1 summarizes $\mathrm{Pos}(C_{N,1})$ and corresponding errors for thickness evaluation. Fig.11 compares Eq. 1 (black) with fitted $\mathrm{Pos}(C_{N,1})$ for the ML-WSe_2 of Fig.1. Solid lines correspond to the mean value and dashed lines indicate position error. We identify Region 1 as $N = 7$ and Region 2 as 10 ± 1.

Table 1. $Pos(C_{N,1})$ and associated fitting errors in ML-WSe_2.

Region	Pos($C_{N,1}$) (cm^{-1})	General fitting error (cm^{-1})	Statistical error (cm^{-1})	Sub-pixel fitting error (cm^{-1})	Total error (cm^{-1})
1	23.76	±0.01	±0.04	±0.06	±0.06
2	24.03	±0.01	±0.01	±0.06	±0.06
bulk	24.38	±0.01	±0.01	±0.06	±0.06

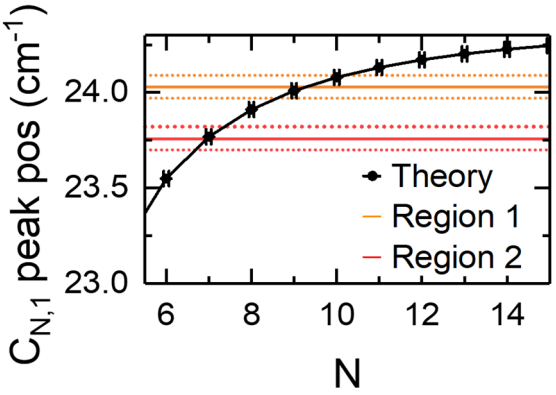

Figure 11. N identification in ML-WSe_2. Black: plot of Eq. 1 based on $Pos(C)_\infty \sim 24.38$ cm^{-1}. Colored solid lines are $Pos(C_{N,1})$ for the ML-WSe_2 regions of Figure 1, with dashed lines indicating the total fitting error.

Time-resolved photoemission electron microscopy. We use a high-repetition-rate, high-power Yb fiber laser (Tangerine 30, Amplitude Systemes), which delivers 40 μJ, 320 fs pulses at 0.6 MHz and 1.03-μm center wavelength (1.20-eV photon energy). After spectral broadening in a Xe-filled hollow-core fiber,[138] a combination of highly dispersive chirped mirrors and a pair of wedges compress pulses to 50 fs FWHM duration. Second and third harmonics, with photon energies ~2.41 and 3.61 eV, are generated through nonlinear frequency conversion in β-barium borate crystals, followed by temporal compression using a prism pair. The FWHM of the second harmonic, which acts as pump beam, is ~46 fs, whereas that of the third harmonic, acting as a probe, is ~40 fs.

The pump beam is sent into a computer-controlled optical delay line to vary the time delay between pump and probe pulses. The overall time resolution, as determined by pump-probe cross-correlation at the sample position, has FWHM~55fs. The PEEM microscope (Focus GmbH, PEEM-IS) has a spatial resolution~77nm according to the 16–84% criterion, defined as the distance over which the image intensity decreases from 84% to 16% of its maximum.[91,139] At each time delay, the image acquisition time is 19 s. The PEEM microscope (Focus GmbH, PEEM-IS) has a spatial resolution~77nm according to the 16–84% criterion, defined as the distance over which the image intensity decreases from 84% to 16% of its maximum.[91,139] At each time delay, the image acquisition time is 19 s. Time-zero is defined as the pump-probe time delay when the peaks of the pump and probe pulse envelopes overlap. It is determined by global fitting of the PEEM signals from 1L- and 7L-WSe_2. This approach determines time-zero with an uncertainty <2 fs. Our measurements employ a time-integrated detector and do not resolve the dynamics of the photoemission process. Thus, the temporal behavior of secondary electron emission does not contribute to the observed pump-probe dynamics.

We now consider possible artifacts associated with surface photovoltage, space-charge, and sample charging effects. Surface photovoltage and space-charge lead to shifts[140] and broadening of the photoemission spectra,[141] respectively. These effects do not affect energy-integrated TR-PEEM measurements, such as ours, consistent with the fact that corrections for these effects in energy-resolved measurements do not affect the total number of photoemitted e.[115,142] For a set of time delays t_i, the data acquisition program collects a PEEM image at t_i, $S(t_i)$, and immediately after that, an image at 250 ps, $S(250_i)$. The differential PEEM signal given by $\Delta S(t_i) = S(t_i) - S(250_i)$. Since the acquisition time of individual images is 19 s, while sample charging builds up over a~1h timescale under our conditions, sample charging is minimized by referencing to the

images collected at 250 ps. As the pump-probe signal is negligible (~0.2% of the peak pump-probe signal) at this 250-ps time delay, this referencing procedure also allows for the removal of one-color multiphoton pump-only and multiphoton probe-only signals. The spatial dependence of the PEEM signal in the 7L-WSe_2 region, shown in Fig.5c and assigned to the depletion width, cannot originate from surface photovoltage, because our energy-integrated measurements are insensitive to energy shifts induced by surface photovoltage.[140]

***Ab Initio* nonadiabatic molecular dynamics.** Simulations based on nonadiabatic molecular dynamics allows us to model quantum transitions between e states responsible for charge transfer and recombination processes accompanied by e-vibrational energy relaxation. Geometry optimization, e structure and adiabatic molecular dynamics simulations are performed with the Vienna *ab initio* simulation package (VASP).[143,144] The Pedrew-Burke-Ernzerhof[145] functional is chosen to describe the e exchange-correlation energy. The projector-augmented wave[146] approach with a 400eV plane-wave basis energy cutoff is used to treat interactions between ionic cores and valence e. The van der Waals interactions are described with the Grimme DFT-D3 method.[147] The periodic images are separated by~15 Å of vacuum perpendicular to the normal of the 1L/2L WSe_2 plane to screen off spurious interactions. Geometry relaxation stops when the ion forces are $<10^{-3}$ $eV \cdot Å^{-1}$.

The nonadiabatic molecular dynamics simulation of the photoinduced charge transfer is performed using the mixed quantum-classical fewest-switches surface hopping technique[148], implemented within the time-dependent Kohn-Sham theory.[134,149] The e densities of edge states excluded from the simulations are in the Supporting Information. The e-h recombination is modelled by the decoherence-induced fewest-switches surface hopping approach,[150] taking into account loss of coherence in the e subsystem induced by coupling to phonons. The decoherence

time is estimated as the pure-dephasing time of the optical response using the second-order cumulant approximation.[151,152] The e densities of edge states excluded from the simulations are in the Supporting Information. After geometry optimization, the system is heated to 300 K using uniform velocity rescaling. Then, a 6ps adiabatic MD trajectory is obtained with a 1 fs time step in the microcanonical ensemble. The trajectory is used to perform the NAMD calculations. In order to model e-h recombination over hundreds ps, the 6-ps NAMD Hamiltonian is iterated under the classical path approximation. Detailed information on the simulation algorithms is in Refs.[153,154]. This methodology was previously used to model excited state dynamics in a broad range of materials, such as semiconductor[155] and metallic[156] quantum dots, nanotubes,[157] metal halide perovskites,[158] plasmonic structures,[159] transition metal oxides,[160] and nanoscale interfaces.[161]

Acknowledgments

We acknowledge funding from the Ministry of Education, Singapore (MOE2018-T2-1-081, MOE-T2EP50221-0004 and RG1/22), the A*STAR Advanced Optics in Engineering Program (122 360 0008), the National Natural Science Foundation of China (21973006), the EU Graphene and Quantum Flagships, ERC grants Hetero2D, GSYNCOR, EPSRC grants EP/L0160871/1, EP/K01711X/1, EP/K017144/1, EP/V000055/1 and the U.S. National Science Foundation (CHE-1900510).

Supporting Information

Supporting Information is available free of charge online. Determination of photon order and probe window, kinetic modeling of TR-PEEM, characterization and TR-PEEM time traces of isolated 1L-WSe_2, analysis of decay amplitudes of 1L-WSe_2, estimation of exciton densities of isolated 1L-WSe_2 and 1L–7L-WSe_2, extraction of depletion width and its time dependence, charge density plots of edge states.

References

(1) Duong, D. L.; Yun, S. J.; Lee, Y. H. Van Der Waals Layered Materials: Opportunities and Challenges. *ACS Nano* **2017**, *11* (12), 11803-11830.

(2) Bhimanapati, G. R.; Lin, Z.; Meunier, V.; Jung, Y.; Cha, J.; Das, S.; Xiao, D.; Son, Y.; Strano, M. S.; Cooper, V. R.; Liang, L.; Louie, S. G.; Ringe, E.; Zhou, W.; Kim, S. S.; Naik, R. R.; Sumpter, B. G.; Terrones, H.; Xia, F.; Wang, Y.; et al. Recent Advances in Two-Dimensional Materials Beyond Graphene. *ACS Nano* **2015**, *9* (12), 11509-11539.

(3) Jariwala, D.; Sangwan, V. K.; Lauhon, L. J.; Marks, T. J.; Hersam, M. C. Emerging Device Applications for Semiconducting Two-Dimensional Transition Metal Dichalcogenides. *ACS Nano* **2014**, *8* (2), 1102-1120.

(4) Butler, S. Z.; Hollen, S. M.; Cao, L.; Cui, Y.; Gupta, J. A.; Gutiérrez, H. R.; Heinz, T. F.; Hong, S. S.; Huang, J.; Ismach, A. F.; Johnston-Halperin, E.; Kuno, M.; Plashnitsa, V. V.; Robinson, R. D.; Ruoff, R. S.; Salahuddin, S.; Shan, J.; Shi, L.; Spencer, M. G.; Terrones, M.; et al. Progress, Challenges, and Opportunities in Two-Dimensional Materials Beyond Graphene. *ACS Nano* **2013**, *7* (4), 2898-2926.

(5) Ferrari, A. C.; Bonaccorso, F.; Fal'ko, V.; Novoselov, K. S.; Roche, S.; Bøggild, P.; Borini, S.; Koppens, F. H. L.; Palermo, V.; Pugno, N.; Garrido, J. A.; Sordan, R.; Bianco, A.; Ballerini, L.; Prato, M.; Lidorikis, E.; Kivioja, J.; Marinelli, C.; Ryhänen, T.; Morpurgo, A.; et al. Science and Technology Roadmap for Graphene, Related Two-Dimensional Crystals, and Hybrid Systems. *Nanoscale* **2015**, *7* (11), 4598-4810.

(6) Bonaccorso, F.; Sun, Z.; Hasan, T.; Ferrari, A. C. Graphene Photonics and Optoelectronics. *Nat. Photonics* **2010**, *4* (9), 611-622.

(7) Koppens, F. H. L.; Mueller, T.; Avouris, P.; Ferrari, A. C.; Vitiello, M. S.; Polini, M. Photodetectors Based on Graphene, Other Two-Dimensional Materials and Hybrid Systems. *Nat. Nanotechnol.* **2014**, *9* (10), 780-793.

(8) Zhao, W.; Ghorannevis, Z.; Chu, L.; Toh, M.; Kloc, C.; Tan, P.-H.; Eda, G. Evolution of Electronic Structure in Atomically Thin Sheets of WS_2 and WSe_2. *ACS Nano* **2013**, *7* (1), 791-797.

(9) Zhang, Y.; Chang, T.-R.; Zhou, B.; Cui, Y.-T.; Yan, H.; Liu, Z.; Schmitt, F.; Lee, J.; Moore, R.; Chen, Y. Direct Observation of the Transition from Indirect to Direct Bandgap in Atomically Thin Epitaxial $MoSe_2$. *Nat. Nanotechnol.* **2014**, *9* (2), 111.

(10) Rezende, N. P.; Cadore, A. R.; Gadelha, A. C.; Pereira, C. L.; Ornelas, V.; Watanabe, K.; Taniguchi, T.; Ferlauto, A. S.; Malachias, A.; Campos, L. C.; Lacerda, R. G. Probing the Electronic Properties of Monolayer MoS_2 Via Interaction with Molecular Hydrogen. *Adv. Electron. Mater.* **2019**, *5* (2), 1800591.

(11) Radisavljevic, B.; Radenovic, A.; Brivio, J.; Giacometti, V.; Kis, A. Single-Layer MoS_2 Transistors. *Nat. Nanotechnol.* **2011**, *6* (3), 147-150.

(12) Radisavljevic, B.; Kis, A. Mobility Engineering and a Metal–Insulator Transition in Monolayer MoS_2. *Nat. Mater.* **2013**, *12* (9), 815-820.

(13) Kang, K.; Xie, S.; Huang, L.; Han, Y.; Huang, P. Y.; Mak, K. F.; Kim, C.-J.; Muller, D.; Park, J. High-Mobility Three-Atom-Thick Semiconducting Films with Wafer-Scale Homogeneity. *Nature* **2015**, *520* (7549), 656-660.

(14) Piatti, E.; De Fazio, D.; Daghero, D.; Tamalampudi, S. R.; Yoon, D.; Ferrari, A. C.; Gonnelli, R. S. Multi-Valley Superconductivity in Ion-Gated MoS_2 Layers. *Nano Lett.* **2018**, *18* (8), 4821-4830.

(15) Orchin, G. J.; De Fazio, D.; Di Bernardo, A.; Hamer, M.; Yoon, D.; Cadore, A. R.; Goykhman, I.; Watanabe, K.; Taniguchi, T.; Robinson, J. W. Niobium Diselenide Superconducting Photodetectors. *Appl. Phys. Lett.* **2019**, *114* (25), 251103.

(16) Barbone, M.; Montblanch, A. R. P.; Kara, D. M.; Palacios-Berraquero, C.; Cadore, A. R.; De Fazio, D.; Pingault, B.; Mostaani, E.; Li, H.; Chen, B.; Watanabe, K.; Taniguchi, T.; Tongay, S.; Wang, G.; Ferrari, A. C.; Atatüre, M. Charge-Tuneable Biexciton Complexes in Monolayer WSe_2. *Nat. Commun.* **2018**, *9* (1), 3721.

(17) Chernikov, A.; Berkelbach, T. C.; Hill, H. M.; Rigosi, A.; Li, Y.; Aslan, O. B.; Reichman, D. R.; Hybertsen, M. S.; Heinz, T. F. Exciton Binding Energy and Nonhydrogenic Rydberg Series in Monolayer WS_2. *Phys. Rev. Lett.* **2014**, *113* (7), 076802.

(18) Bellus, M. Z.; Ceballos, F.; Chiu, H.-Y.; Zhao, H. Tightly Bound Trions in Transition Metal Dichalcogenide Heterostructures. *ACS Nano* **2015**, *9* (6), 6459-6464.

(19) Mostaani, E.; Szyniszewski, M.; Price, C. H.; Maezono, R.; Danovich, M.; Hunt, R. J.; Drummond, N. D.; Fal'ko, V. I. Diffusion Quantum Monte Carlo Study of Excitonic Complexes in Two-Dimensional Transition-Metal Dichalcogenides. *Phys. Rev. B* **2017**, *96* (7), 075431.

(20) Klimmer, S.; Ghaebi, O.; Gan, Z.; George, A.; Turchanin, A.; Cerullo, G.; Soavi, G. All-Optical Polarization and Amplitude Modulation of Second-Harmonic Generation in Atomically Thin Semiconductors. *Nat. Photonics* **2021**, *15* (11), 837-842.

(21) Soavi, G.; Wang, G.; Rostami, H.; Purdie, D. G.; De Fazio, D.; Ma, T.; Luo, B.; Wang, J.; Ott, A. K.; Yoon, D.; Bourelle, S. A.; Muench, J. E.; Goykhman, I.; Dal Conte, S.; Celebrano, M.; Tomadin, A.; Polini, M.; Cerullo, G.; Ferrari, A. C. Broadband, Electrically Tunable Third-Harmonic Generation in Graphene. *Nat. Nanotechnol.* **2018**, *13* (7), 583-588.

(22) Bikorimana, S.; Lama, P.; Walser, A.; Dorsinville, R.; Anghel, S.; Mitioglu, A.; Micu, A.; Kulyuk, L. Nonlinear Optical Responses in Two-Dimensional Transition Metal Dichalcogenide Multilayer: WS_2, WSe_2, MoS_2 and $Mo_{0.5}W_{0.5}S_2$. *Opt. Express* **2016**, *24* (18), 20685-20695.

(23) Säynätjoki, A.; Karvonen, L.; Rostami, H.; Autere, A.; Mehravar, S.; Lombardo, A.; Norwood, R. A.; Hasan, T.; Peyghambarian, N.; Lipsanen, H.; Kieu, K.; Ferrari, A. C.; Polini, M.; Sun, Z. Ultra-Strong Nonlinear Optical Processes and Trigonal Warping in MoS_2 Layers. *Nat. Commun.* **2017**, *8* (1), 893.

(24) Lafeta, L.; Corradi, A.; Zhang, T.; Kahn, E.; Bilgin, I.; Carvalho, B. R.; Kar, S.; Terrones, M.; Malard, L. M. Second- and Third-Order Optical Susceptibilities across Excitons States in 2D Monolayer Transition Metal Dichalcogenides. *2D Mater.* **2021**, *8* (3), 035010.

(25) Scarpelli, L.; Masia, F.; Alexeev, E. M.; Withers, F.; Tartakovskii, A. I.; Novoselov, K. S.; Langbein, W. Resonantly Excited Exciton Dynamics in Two-Dimensional $MoSe_2$ Monolayers. *Phys. Rev. B* **2017**, *96* (4), 045407.

(26) Wang, G.; Chernikov, A.; Glazov, M. M.; Heinz, T. F.; Marie, X.; Amand, T.; Urbaszek, B. Colloquium: Excitons in Atomically Thin Transition Metal Dichalcogenides. *Rev. Mod. Phys.* **2018**, *90* (2), 021001.

(27) Trovatello, C.; Miranda, H. P. C.; Molina-Sánchez, A.; Borrego-Varillas, R.; Manzoni, C.; Moretti, L.; Ganzer, L.; Maiuri, M.; Wang, J.; Dumcenco, D.; Kis, A.; Wirtz, L.; Marini, A.; Soavi, G.; Ferrari, A. C.; Cerullo, G.; Sangalli, D.; Conte, S. D. Strongly Coupled Coherent Phonons in Single-Layer MoS_2. *ACS Nano* **2020**, *14* (5), 5700-5710.

(28) Paradisanos, I.; Wang, G.; Alexeev, E. M.; Cadore, A. R.; Marie, X.; Ferrari, A. C.; Glazov, M. M.; Urbaszek, B. Efficient Phonon Cascades in WSe_2 Monolayers. *Nat. Commun.* **2021**, *12* (1), 538.

(29) Li, D.; Trovatello, C.; Dal Conte, S.; Nuß, M.; Soavi, G.; Wang, G.; Ferrari, A. C.; Cerullo, G.; Brixner, T. Exciton–Phonon Coupling Strength in Single-Layer $MoSe_2$ at Room Temperature. *Nat. Commun.* **2021**, *12* (1), 954.

(30) Bonaccorso, F.; Lombardo, A.; Hasan, T.; Sun, Z.; Ferrari, A. C. Production and Processing of Graphene and 2D Crystals. *Mater. Today* **2012**, *15* (12), 564–589.

(31) Choi, W.; Choudhary, N.; Gang, H. H.; Park, J.; Akinwande, D.; Lee, Y. H. Recent Development of Two-Dimensional Transition Metal Dichalcogenides and Their Applications. *Mater. Today* **2017**, *20* (3), 116-130.

(32) Backes, C.; Abdelkader, A. M.; Alonso, C.; Andrieux-Ledier, A.; Arenal, R.; Azpeitia, J.; Balakrishnan, N.; Banszerus, L.; Barjon, J.; Bartali, R.; Bellani, S.; Berger, C.; Berger, R.; Ortega, M. M. B.; Bernard, C.; Beton, P. H.; Beyer, A.; Bianco, A.; Bøggild, P.; Bonaccorso, F.; et al. Production and Processing of Graphene and Related Materials. *2D Mater.* **2020**, *7* (2), 022001.

(33) De Fazio, D.; Goykhman, I.; Yoon, D.; Bruna, M.; Eiden, A.; Milana, S.; Sassi, U.; Barbone, M.; Dumcenco, D.; Marinov, K.; Kis, A.; Ferrari, A. C. High Responsivity, Large-Area Graphene/MoS_2 Flexible Photodetectors. *ACS Nano* **2016**, *10* (9), 8252-8262.

(34) Huo, N.; Konstantatos, G. Ultrasensitive All-2D MoS_2 Phototransistors Enabled by an out-of-Plane MoS_2 Pn Homojunction. *Nat. Commun.* **2017**, *8* (1), 572.

(35) Gadelha, A. C.; Cadore, A. R.; Watanabe, K.; Taniguchi, T.; de Paula, A. M.; Malard, L. M.; Lacerda, R. G.; Campos, L. C. Gate-Tunable Non-Volatile Photomemory Effect in MoS_2 Transistors. *2D Mater.* **2019**, *6* (2), 025036.

(36) Sundaram, R.; Engel, M.; Lombardo, A.; Krupke, R.; Ferrari, A.; Avouris, P.; Steiner, M. Electroluminescence in Single Layer MoS_2. *Nano Lett.* **2013**, *13* (4), 1416-1421.

(37) Palacios-Berraquero, C.; Barbone, M.; Kara, D. M.; Chen, X.; Goykhman, I.; Yoon, D.; Ott, A. K.; Beitner, J.; Watanabe, K.; Taniguchi, T.; Ferrari, A. C.; Atatüre, M. Atomically Thin Quantum Light-Emitting Diodes. *Nat. Commun.* **2016**, *7* (1), 12978.

(38) Wang, J.; Verzhbitskiy, I.; Eda, G. Electroluminescent Devices Based on 2D Semiconducting Transition Metal Dichalcogenides. *Adv. Mater.* **2018**, *30* (47), 1802687.

(39) Peña Román, R. J.; Auad, Y.; Grasso, L.; Alvarez, F.; Barcelos, I. D.; Zagonel, L. F. Tunneling-Current-Induced Local Excitonic Luminescence in p-Doped WSe_2 Monolayers. *Nanoscale* **2020**, *12* (25), 13460-13470.

(40) Manzeli, S.; Ovchinnikov, D.; Pasquier, D.; Yazyev, O. V.; Kis, A. 2D Transition Metal Dichalcogenides. *Nat. Rev. Mater.* **2017**, *2* (8), 17033.

(41) Zhang, X.-Q.; Lin, C.-H.; Tseng, Y.-W.; Huang, K.-H.; Lee, Y.-H. Synthesis of Lateral Heterostructures of Semiconducting Atomic Layers. *Nano Lett.* **2015**, *15* (1), 410-415.

(42) Liu, Y.; Weiss, N. O.; Duan, X.; Cheng, H.-C.; Huang, Y.; Duan, X. Van Der Waals Heterostructures and Devices. *Nat. Rev. Mater.* **2016**, *1* (9), 1-17.

(43) Shinde, S. M.; Dhakal, K. P.; Chen, X.; Yun, W. S.; Lee, J.; Kim, H.; Ahn, J.-H. Stacking-Controllable Interlayer Coupling and Symmetric Configuration of Multilayered MoS_2. *NPG Asia Materials* **2018**, *10* (2), e468-e468.

(44) Sahoo, P. K.; Memaran, S.; Xin, Y.; Balicas, L.; Gutiérrez, H. R. One-Pot Growth of Two-Dimensional Lateral Heterostructures Via Sequential Edge-Epitaxy. *Nature* **2018**, *553* (7686), 63-67.

(45) Komsa, H.-P.; Krasheninnikov, A. V. Electronic Structures and Optical Properties of Realistic Transition Metal Dichalcogenide Heterostructures from First Principles. *Phys. Rev. B* **2013**, *88* (8), 085318.

(46) Gong, Y.; Lei, S.; Ye, G.; Li, B.; He, Y.; Keyshar, K.; Zhang, X.; Wang, Q.; Lou, J.; Liu, Z. Two-Step Growth of Two-Dimensional WSe_2/$MoSe_2$ Heterostructures. *Nano Lett.* **2015**, *15* (9), 6135-6141.

(47) Furchi, M. M.; Pospischil, A.; Libisch, F.; Burgdörfer, J.; Mueller, T. Photovoltaic Effect in an Electrically Tunable Van Der Waals Heterojunction. *Nano Lett.* **2014**, *14* (8), 4785-4791.

(48) Sahoo, P. K.; Memaran, S.; Nugera, F. A.; Xin, Y.; Díaz Márquez, T.; Lu, Z.; Zheng, W.; Zhigadlo, N. D.; Smirnov, D.; Balicas, L.; Gutiérrez, H. R. Bilayer Lateral Heterostructures of Transition-Metal Dichalcogenides and Their Optoelectronic Response. *ACS Nano* **2019**, *13* (11), 12372-12384.

(49) Huo, N.; Kang, J.; Wei, Z.; Li, S.-S.; Li, J.; Wei, S.-H. Novel and Enhanced Optoelectronic Performances of Multilayer MoS_2–WS_2 Heterostructure Transistors. *Adv. Funct. Mater.* **2014**, *24* (44), 7025-7031.

(50) Huo, N.; Tongay, S.; Guo, W.; Li, R.; Fan, C.; Lu, F.; Yang, J.; Li, B.; Li, Y.; Wei, Z. Novel Optical and Electrical Transport Properties in Atomically Thin WSe_2/MoS_2 p–n Heterostructures. *Adv. Electron. Mater.* **2015**, *1* (5), 1400066.

(51) Jauregui, L. A.; Joe, A. Y.; Pistunova, K.; Wild, D. S.; High, A. A.; Zhou, Y.; Scuri, G.; De Greve, K.; Sushko, A.; Yu, C.-H.; Taniguchi, T.; Watanabe, K.; Needleman, D. J.; Lukin, M. D.; Park, H.; Kim, P. Electrical Control of Interlayer Exciton Dynamics in Atomically Thin Heterostructures. *Science* **2019**, *366* (6467), 870-875.

(52) Ruiz-Tijerina, D. A.; Fal'ko, V. I. Interlayer Hybridization and Moiré Superlattice Minibands for Electrons and Excitons in Heterobilayers of Transition-Metal Dichalcogenides. *Phys. Rev. B* **2019**, *99* (12), 125424.

(53) Alexeev, E. M.; Ruiz-Tijerina, D. A.; Danovich, M.; Hamer, M. J.; Terry, D. J.; Nayak, P. K.; Ahn, S.; Pak, S.; Lee, J.; Sohn, J. I.; Molas, M. R.; Koperski, M.; Watanabe, K.; Taniguchi, T.; Novoselov, K. S.; Gorbachev, R. V.; Shin, H. S.; Fal'ko, V. I.; Tartakovskii, A. I. Resonantly Hybridized Excitons in Moiré Superlattices in Van Der Waals Heterostructures. *Nature* **2019**, *567* (7746), 81-86.

(54) Montblanch, A. R. P.; Kara, D. M.; Paradisanos, I.; Purser, C. M.; Feuer, M. S. G.; Alexeev, E. M.; Stefan, L.; Qin, Y.; Blei, M.; Wang, G.; Cadore, A. R.; Latawiec, P.; Lončar, M.; Tongay, S.; Ferrari, A. C.; Atatüre, M. Confinement of Long-Lived Interlayer Excitons in WS_2/WSe_2 Heterostructures. *Commun. Phys.* **2021**, *4* (1), 119.

(55) Paradisanos, I.; Shree, S.; George, A.; Leisgang, N.; Robert, C.; Watanabe, K.; Taniguchi, T.; Warburton, R. J.; Turchanin, A.; Marie, X.; Gerber, I. C.; Urbaszek, B. Controlling Interlayer Excitons in MoS_2 Layers Grown by Chemical Vapor Deposition. *Nat. Commun.* **2020**, *11* (1), 2391.

(56) Gong, C.; Zhang, H.; Wang, W.; Colombo, L.; Wallace, R. M.; Cho, K. Band Alignment of Two-Dimensional Transition Metal Dichalcogenides: Application in Tunnel Field Effect Transistors. *Appl. Phys. Lett.* **2013**, *103* (5), 053513.

(57) Chiu, M.-H.; Zhang, C.; Shiu, H.-W.; Chuu, C.-P.; Chen, C.-H.; Chang, C.-Y. S.; Chen, C.-H.; Chou, M.-Y.; Shih, C.-K.; Li, L.-J. Determination of Band Alignment in the Single-Layer MoS_2/WSe_2 Heterojunction. *Nat. Commun.* **2015**, *6*, 7666.

(58) Guo, Y.; Robertson, J. Band Engineering in Transition Metal Dichalcogenides: Stacked Versus Lateral Heterostructures. *Appl. Phys. Lett.* **2016**, *108* (23), 233104.

(59) Bellus, M. Z.; Li, M.; Lane, S. D.; Ceballos, F.; Cui, Q.; Zeng, X. C.; Zhao, H. Type-I Van Der Waals Heterostructure Formed by MoS_2 and Res_2 Monolayers. *Nanoscale Horiz.* **2017**, *2* (1), 31-36.

(60) Ross, J. S.; Rivera, P.; Schaibley, J.; Lee-Wong, E.; Yu, H.; Taniguchi, T.; Watanabe, K.; Yan, J.; Mandrus, D.; Cobden, D. Interlayer Exciton Optoelectronics in a 2D Heterostructure p–n Junction. *Nano Lett.* **2017**, *17* (2), 638-643.

(61) Ceballos, F.; Bellus, M. Z.; Chiu, H.-Y.; Zhao, H. Ultrafast Charge Separation and Indirect Exciton Formation in a MoS_2–$MoSe_2$ Van Der Waals Heterostructure. *ACS Nano* **2014**, *8* (12), 12717-12724.

(62) Hong, X.; Kim, J.; Shi, S.-F.; Zhang, Y.; Jin, C.; Sun, Y.; Tongay, S.; Wu, J.; Zhang, Y.; Wang, F. Ultrafast Charge Transfer in Atomically Thin MoS_2/WS_2 Heterostructures. *Nat. Nanotechnol.* **2014**, *9* (9), 682-686.

(63) Chen, H.; Wen, X.; Zhang, J.; Wu, T.; Gong, Y.; Zhang, X.; Yuan, J.; Yi, C.; Lou, J.; Ajayan, P. M.; Zhuang, W.; Zhang, G.; Zheng, J. Ultrafast Formation of Interlayer Hot Excitons in Atomically Thin MoS_2/WS_2 Heterostructures. *Nat. Commun.* **2016**, *7*, 12512.

(64) Zhu, H. M.; Wang, J.; Gong, Z. Z.; Kim, Y. D.; Hone, J.; Zhu, X. Y. Interfacial Charge Transfer Circumventing Momentum Mismatch at Two-Dimensional Van Der Waals Heterojunctions. *Nano Lett.* **2017**, *17* (6), 3591-3598.

(65) Ji, Z. H.; Hong, H.; Zhang, J.; Zhang, Q.; Huang, W.; Cao, T.; Qiao, R. X.; Liu, C.; Liang, J.; Jin, C. H.; Jiao, L. Y.; Shi, K. B.; Meng, S.; Liu, K. H. Robust Stacking-Independent Ultrafast Charge Transfer in MoS_2/WS_2 Bilayers. *ACS Nano* **2017**, *11* (12), 12020-12026.

(66) Jin, C. H.; Ma, E. Y.; Karni, O.; Regan, E. C.; Wang, F.; Heinz, T. F. Ultrafast Dynamics in Van Der Waals Heterostructures. *Nat. Nanotechnol.* **2018**, *13* (11), 994-1003.

(67) Zhou, H. Z.; Zhao, Y. D.; Zhu, H. M. Dielectric Environment-Robust Ultrafast Charge Transfer between Two Atomic Layers. *J. Phys. Chem. Lett.* **2019**, *10* (2), 150-155.

(68) Long, R.; Prezhdo, O. V. Quantum Coherence Facilitates Efficient Charge Separation at a MoS_2/$MoSe_2$ Van Der Waals Junction. *Nano Lett.* **2016**, *16* (3), 1996-2003, Article.

(69) Wang, Y.; Wang, Z.; Yao, W.; Liu, G.-B.; Yu, H. Interlayer Coupling in Commensurate and Incommensurate Bilayer Structures of Transition-Metal Dichalcogenides. *Phys. Rev. B* **2017**, *95* (11), 115429.

(70) Bellus, M. Z.; Mahjouri-Samani, M.; Lane, S. D.; Oyedele, A. D.; Li, X.; Puretzky, A. A.; Geohegan, D.; Xiao, K.; Zhao, H. Photocarrier Transfer across Monolayer MoS_2–$MoSe_2$ Lateral Heterojunctions. *ACS Nano* **2018**, *12* (7), 7086-7092.

(71) Hao, H.; Xu, Z.; Jiang, T.; Wei, K.; Li, H.; Zheng, X.; Yin, K.; You, J.; Shen, C.; Cheng, X.-a. Visualized Charge Transfer Processes in Monolayer Composition-Graded $Ws_{2x}se_{2(1-X)}$ Lateral Heterojunctions Via Ultrafast Microscopy Mapping. *Opt. Express* **2018**, *26* (12), 15867-15886.
(72) Howell, S. L.; Jariwala, D.; Wu, C.-C.; Chen, K.-S.; Sangwan, V. K.; Kang, J.; Marks, T. J.; Hersam, M. C.; Lauhon, L. J. Investigation of Band-Offsets at Monolayer–Multilayer MoS_2 Junctions by Scanning Photocurrent Microscopy. *Nano Lett.* **2015**, *15* (4), 2278-2284.
(73) Xu, Z.-Q.; Zhang, Y.; Wang, Z.; Shen, Y.; Huang, W.; Xia, X.; Yu, W.; Xue, Y.; Sun, L.; Zheng, C.; Lu, Y.; Liao, L.; Bao, Q. Atomically Thin Lateral p–n Junction Photodetector with Large Effective Detection Area. *2D Mater.* **2016**, *3* (4), 041001.
(74) Sun, M.; Xie, D.; Sun, Y.; Li, W.; Teng, C.; Xu, J. Lateral Multilayer/Monolayer MoS_2 Heterojunction for High Performance Photodetector Applications. *Sci. Rep.* **2017**, *7* (1), 4505.
(75) Xia, C.; Xiong, W.; Du, J.; Wang, T.; Peng, Y.; Wei, Z.; Li, J.; Jia, Y. Type-I Transition Metal Dichalcogenides Lateral Homojunctions: Layer Thickness and External Electric Field Effects. *Small* **2018**, *14* (21), e1800365.
(76) Jia, Z.; Shi, J.; Shang, Q.; Du, W.; Shan, X.; Ge, B.; Li, J.; Sui, X.; Zhong, Y.; Wang, Q.; Bao, L.; Zhang, Q.; Liu, X. Charge-Transfer-Induced Photoluminescence Properties of WSe_2 Monolayer–Bilayer Homojunction. *ACS Appl. Mater. Interfaces* **2019**, *11* (22), 20566-20573.
(77) Wu, J. J.; Peng, J.; Zhou, Y.; Lin, Y.; Wen, X. L.; Wu, J. C.; Zhao, Y. C.; Guo, Y. Q.; Wu, C. Z.; Xie, Y. Solution Processing for Lateral Transition-Metal Dichalcogenides Homojunction from Polymorphic Crystal. *J. Am. Chem. Soc.* **2019**, *141* (1), 592-598.
(78) Wu, G. J.; Tian, B. B.; Liu, L.; Lv, W.; Wu, S.; Wang, X. D.; Chen, Y.; Li, J. Y.; Wang, Z.; Wu, S. Q.; Shen, H.; Lin, T.; Zhou, P.; Liu, Q.; Duan, C. G.; Zhang, S. T.; Meng, X. J.; Wu, S. W.; Hu, W. D.; Wang, X. R.; et al. Programmable Transition Metal Dichalcogenide Homojunctions Controlled by Nonvolatile Ferroelectric Domains. *Nat. Electron.* **2020**, *3* (1), 43-50.
(79) Utama, M. I. B.; Kleemann, H.; Zhao, W. Y.; Ong, C. S.; da Jornada, F. H.; Qiu, D. Y.; Cai, H.; Li, H.; Kou, R.; Zhao, S. H.; Wang, S.; Watanabe, K.; Taniguchi, T.; Tongay, S.; Zettl, A.; Louie, S. G.; Wang, F. A Dielectric-Defined Lateral Heterojunction in a Monolayer Semiconductor. *Nat. Electron.* **2019**, *2* (2), 60-65.
(80) Zhang, C.; Chen, Y.; Huang, J.-K.; Wu, X.; Li, L.-J.; Yao, W.; Tersoff, J.; Shih, C.-K. Visualizing Band Offsets and Edge States in Bilayer–Monolayer Transition Metal Dichalcogenides Lateral Heterojunction. *Nat. Commun.* **2016**, *7*, 10349.

(81) Fang, L.; Yuan, X.; Liu, K.; Li, L.; Zhou, P.; Ma, W.; Huang, H.; He, J.; Tao, S. Direct Bilayer Growth: A New Growth Principle for a Novel WSe_2 Homo-Junction and Bilayer WSe_2 Growth. *Nanoscale* **2020**, *12* (6), 3715-3722.
(82) Mak, K. F.; Lee, C.; Hone, J.; Shan, J.; Heinz, T. F. Atomically Thin MoS_2: A New Direct-Gap Semiconductor. *Phys. Rev. Lett.* **2010**, *105* (13), 136805.
(83) Splendiani, A.; Sun, L.; Zhang, Y.; Li, T.; Kim, J.; Chim, C.-Y.; Galli, G.; Wang, F. Emerging Photoluminescence in Monolayer MoS_2. *Nano Lett.* **2010**, *10* (4), 1271-1275.
(84) Zeng, H.; Liu, G.-B.; Dai, J.; Yan, Y.; Zhu, B.; He, R.; Xie, L.; Xu, S.; Chen, X.; Yao, W. Optical Signature of Symmetry Variations and Spin-Valley Coupling in Atomically Thin Tungsten Dichalcogenides. *Sci. Rep.* **2013**, *3*, 1608.
(85) Tosun, M.; Fu, D. Y.; Desai, S. B.; Ko, C.; Kang, J. S.; Lien, D. H.; Najmzadeh, M.; Tongay, S.; Wu, J. Q.; Javey, A. MoS_2 Heterojunctions by Thickness Modulation. *Sci. Rep.* **2015**, *5*, 10990.
(86) Novoselov, K. S.; Jiang, D.; Schedin, F.; Booth, T. J.; Khotkevich, V. V.; Morozov, S. V.; Geim, A. K. Two-Dimensional Atomic Crystals. *Proc. Natl. Acad. Sci. U.S.A.* **2005**, *102* (30), 10451-10453.
(87) Jarrett, J. W.; Zhao, T.; Johnson, J. S.; Knappenberger, K. L. Investigating Plasmonic Structure-Dependent Light Amplification and Electronic Dynamics Using Advances in Nonlinear Optical Microscopy. *J. Phys. Chem. C* **2015**, *119* (28), 15779-15800.
(88) Beane, G.; Devkota, T.; Brown, B. S.; Hartland, G. V. Ultrafast Measurements of the Dynamics of Single Nanostructures: A Review. *Rep. Prog. Phys.* **2019**, *82* (1), 016401.
(89) Zhu, T.; Snaider, J. M.; Yuan, L.; Huang, L. Ultrafast Dynamic Microscopy of Carrier and Exciton Transport. *Annu. Rev. Phys. Chem.* **2019**, *70* (1), 219-244.
(90) Fukumoto, K.; Onda, K.; Yamada, Y.; Matsuki, T.; Mukuta, T.; Tanaka, S.-i.; Koshihara, S.-y. Femtosecond Time-Resolved Photoemission Electron Microscopy for Spatiotemporal Imaging of Photogenerated Carrier Dynamics in Semiconductors. *Rev. Sci. Instrum.* **2014**, *85* (8), 083705.
(91) Doherty, T. A. S.; Winchester, A. J.; Macpherson, S.; Johnstone, D. N.; Pareek, V.; Tennyson, E. M.; Kosar, S.; Kosasih, F. U.; Anaya, M.; Abdi-Jalebi, M.; Andaji-Garmaroudi, Z.; Wong, E. L.; Madéo, J.; Chiang, Y.-H.; Park, J.-S.; Jung, Y.-K.; Petoukhoff, C. E.; Divitini, G.; Man, M. K. L.; Ducati, C.; et al. Performance-Limiting Nanoscale Trap Clusters at Grain Junctions in Halide Perovskites. *Nature* **2020**, *580* (7803), 360-366.

(92) Fukumoto, K.; Yamada, Y.; Onda, K.; Koshihara, S.-y. Direct Imaging of Electron Recombination and Transport on a Semiconductor Surface by Femtosecond Time-Resolved Photoemission Electron Microscopy. *Appl. Phys. Lett.* **2014**, *104* (5), 053117.
(93) Man, M. K.; Margiolakis, A.; Deckoff-Jones, S.; Harada, T.; Wong, E. L.; Krishna, M. B. M.; Madéo, J.; Winchester, A.; Lei, S.; Vajtai, R. Imaging the Motion of Electrons across Semiconductor Heterojunctions. *Nat. Nanotechnol.* **2017**, *12* (1), 36.
(94) Wang, L.; Xu, C.; Li, M. Y.; Li, L. J.; Loh, Z.-H. Unraveling Spatially Heterogeneous Ultrafast Carrier Dynamics of Single-Layer WSe_2 by Femtosecond Time-Resolved Photoemission Electron Microscopy. *Nano Lett.* **2018**, *18* (8), 5172-5178.
(95) Xu, C.; Yong, H. W.; He, J.; Long, R.; Cadore, A. R.; Paradisanos, I.; Ott, A. K.; Soavi, G.; Tongay, S.; Cerullo, G.; Ferrari, A. C.; Prezhdo, O. V.; Loh, Z.-H. Weak Distance Dependence of Hot-Electron-Transfer Rates at the Interface between Monolayer MoS_2 and Gold. *ACS Nano* **2021**, *15* (1), 819-828.
(96) Castellanos-Gomez, A.; Buscema, M.; Molenaar, R.; Singh, V.; Janssen, L.; van der Zant, H. S. J.; Steele, G. A. Deterministic Transfer of Two-Dimensional Materials by All-Dry Viscoelastic Stamping. *2D Mater.* **2014**, *1* (1), 011002.
(97) Casiraghi, C.; Hartschuh, A.; Lidorikis, E.; Qian, H.; Harutyunyan, H.; Gokus, T.; Novoselov, K. S.; Ferrari, A. C. Rayleigh Imaging of Graphene and Graphene Layers. *Nano Lett.* **2007**, *7* (9), 2711-2717.
(98) Ferrari, A. C.; Basko, D. M. Raman Spectroscopy as a Versatile Tool for Studying the Properties of Graphene. *Nat. Nanotechnol.* **2013**, *8* (4), 235-246.
(99) Tan, P. H.; Han, W. P.; Zhao, W. J.; Wu, Z. H.; Chang, K.; Wang, H.; Wang, Y. F.; Bonini, N.; Marzari, N.; Pugno, N.; Savini, G.; Lombardo, A.; Ferrari, A. C. The Shear Mode of Multilayer Graphene. *Nat. Mater.* **2012**, *11* (4), 294-300.
(100) Zhang, X.; Han, W. P.; Wu, J. B.; Milana, S.; Lu, Y.; Li, Q. Q.; Ferrari, A. C.; Tan, P. H. Raman Spectroscopy of Shear and Layer Breathing Modes in Multilayer MoS_2. *Phys. Rev. B* **2013**, *87* (11), 115413.
(101) Pizzi, G.; Milana, S.; Ferrari, A. C.; Marzari, N.; Gibertini, M. Shear and Breathing Modes of Layered Materials. *ACS Nano* **2021**, *15* (8), 12509-12534.
(102) Molas, M. R.; Tyurnina, A. V.; Zólyomi, V.; Ott, A. K.; Terry, D. J.; Hamer, M. J.; Yelgel, C.; Babiński, A.; Nasibulin, A. G.; Ferrari, A. C.; Fal'ko, V. I.; Gorbachev, R. Raman

Spectroscopy of Gase and Inse Post-Transition Metal Chalcogenides Layers. *Faraday Discuss.* **2021**, *227* (0), 163-170.

(103) Zhao, W.; Ghorannevis, Z.; Amara, K. K.; Pang, J. R.; Toh, M.; Zhang, X.; Kloc, C.; Tan, P. H.; Eda, G. Lattice Dynamics in Mono- and Few-Layer Sheets of WS_2 and WSe_2. *Nanoscale* **2013**, *5* (20), 9677-9683.

(104) Terrones, H.; Corro, E. D.; Feng, S.; Poumirol, J. M.; Rhodes, D.; Smirnov, D.; Pradhan, N. R.; Lin, Z.; Nguyen, M. A. T.; Elías, A. L.; Mallouk, T. E.; Balicas, L.; Pimenta, M. A.; Terrones, M. New First Order Raman-Active Modes in Few Layered Transition Metal Dichalcogenides. *Sci. Rep.* **2014**, *4* (1), 4215.

(105) del Corro, E.; Terrones, H.; Elias, A.; Fantini, C.; Feng, S.; Nguyen, M. A.; Mallouk, T. E.; Terrones, M.; Pimenta, M. A. Excited Excitonic States in 1L, 2L, 3L, and Bulk WSe_2 Observed by Resonant Raman Spectroscopy. *ACS Nano* **2014**, *8* (9), 9629-9635.

(106) Shi, W.; Lin, M.-L.; Tan, Q.-H.; Qiao, X.-F.; Zhang, J.; Tan, P.-H. Raman and Photoluminescence Spectra of Two-Dimensional Nanocrystallites of Monolayer WS_2 and WSe_2. *2D Mater.* **2016**, *3* (2), 025016.

(107) dos Santos, E. P.; Silva, F. L. R.; Gontijo, R. N.; Alves, J. M.; Ammar, M.-R.; Fantini, C. Temperature Dependence of the Double-Resonance Raman Bands in Bilayer WSe_2. *Vib. Spectrosc* **2020**, *110*, 103117.

(108) Huang, W.; Luo, X.; Gan, C. K.; Quek, S. Y.; Liang, G. Theoretical Study of Thermoelectric Properties of Few-Layer MoS_2 and WSe_2. *Phys. Chem. Chem. Phys.* **2014**, *16* (22), 10866-10874.

(109) Kim, H.-g.; Choi, H. J. Thickness Dependence of Work Function, Ionization Energy, and Electron Affinity of Mo and W Dichalcogenides from DFT and GW Calculations. *Phys. Rev. B* **2021**, *103* (8), 085404.

(110) Nie, Z.; Long, R.; Sun, L.; Huang, C.-C.; Zhang, J.; Xiong, Q.; Hewak, D. W.; Shen, Z.; Prezhdo, O. V.; Loh, Z.-H. Ultrafast Carrier Thermalization and Cooling Dynamics in Few-Layer MoS_2. *ACS Nano* **2014**, *8* (10), 10931-10940.

(111) Li, A.; James, N. A.; Wang, T.; Wang, Z.; Petek, H.; Reutzel, M. Towards Full Surface Brillouin Zone Mapping by Coherent Multi-Photon Photoemission. *New J. Phys.* **2020**, *22* (7), 073035.

(112) Hüfner, S.; *Photoelectron Spectroscopy: Principles and Applications*, 3rd ed.; Springer-Verlag: Berlin, 2003.

(113) Keyshar, K.; Berg, M.; Zhang, X.; Vajtai, R.; Gupta, G.; Chan, C. K.; Beechem, T. E.; Ajayan, P. M.; Mohite, A. D.; Ohta, T. Experimental Determination of the Ionization Energies of $MoSe_2$, WS_2, and MoS_2 on SiO_2 Using Photoemission Electron Microscopy. *ACS Nano* **2017**, *11* (8), 8223-8230.

(114) Wallauer, R.; Perea-Causin, R.; Münster, L.; Zajusch, S.; Brem, S.; Güdde, J.; Tanimura, K.; Lin, K.-Q.; Huber, R.; Malic, E.; Höfer, U. Momentum-Resolved Observation of Exciton Formation Dynamics in Monolayer WS_2. *Nano Lett.* **2021**, *21* (13), 5867-5873.

(115) Madéo, J.; Man, M. K. L.; Sahoo, C.; Campbell, M.; Pareek, V.; Wong, E. L.; Al-Mahboob, A.; Chan, N. S.; Karmakar, A.; Mariserla, B. M. K.; Li, X.; Heinz, T. F.; Cao, T.; Dani, K. M. Directly Visualizing the Momentum-Forbidden Dark Excitons and Their Dynamics in Atomically Thin Semiconductors. *Science* **2020**, *370* (6521), 1199-1204.

(116) Yuan, L.; Huang, L. Exciton Dynamics and Annihilation in WS_2 2D Semiconductors. *Nanoscale* **2015**, *7* (16), 7402-7408.

(117) Sun, D.; Rao, Y.; Reider, G. A.; Chen, G.; You, Y.; Brézin, L.; Harutyunyan, A. R.; Heinz, T. F. Observation of Rapid Exciton–Exciton Annihilation in Monolayer Molybdenum Disulfide. *Nano Lett.* **2014**, *14* (10), 5625-5629.

(118) Poellmann, C.; Steinleitner, P.; Leierseder, U.; Nagler, P.; Plechinger, G.; Porer, M.; Bratschitsch, R.; Schuller, C.; Korn, T.; Huber, R. Resonant Internal Quantum Transitions and Femtosecond Radiative Decay of Excitons in Monolayer WSe_2. *Nat. Mater.* **2015**, *14* (9), 889–893

(119) Rasmussen, F. A.; Thygesen, K. S. Computational 2D Materials Database: Electronic Structure of Transition-Metal Dichalcogenides and Oxides. *J. Phys. Chem. C* **2015**, *119* (23), 13169-13183.

(120) Xuan, F.; Quek, S. Y. Valley Zeeman Effect and Landau Levels in Two-Dimensional Transition Metal Dichalcogenides. *Phys. Rev. Res.* **2020**, *2* (3), 033256.

(121) Mouri, S.; Miyauchi, Y.; Toh, M.; Zhao, W.; Eda, G.; Matsuda, K. Nonlinear Photoluminescence in Atomically Thin Layered WSe_2 Arising from Diffusion-Assisted Exciton-Exciton Annihilation. *Phys. Rev. B* **2014**, *90* (15), 155449.

(122) Kumar, N.; Cui, Q.; Ceballos, F.; He, D.; Wang, Y.; Zhao, H. Exciton-Exciton Annihilation in $MoSe_2$ Monolayers. *Phys. Rev. B* **2014**, *89* (12), 125427.

(123) Raja, A.; Selig, M.; Berghäuser, G.; Yu, J.; Hill, H. M.; Rigosi, A. F.; Brus, L. E.; Knorr, A.; Heinz, T. F.; Malic, E.; Chernikov, A. Enhancement of Exciton–Phonon Scattering from Monolayer to Bilayer WS_2. *Nano Lett.* **2018**, *18* (10), 6135-6143.
(124) Demtröder, W.; *Laser Spectroscopy*, 4th ed.; Springer-Verlag: Berlin, 2008; Vol. 1.
(125) Moody, G.; Kavir Dass, C.; Hao, K.; Chen, C.-H.; Li, L.-J.; Singh, A.; Tran, K.; Clark, G.; Xu, X.; Berghäuser, G.; Malic, E.; Knorr, A.; Li, X. Intrinsic Homogeneous Linewidth and Broadening Mechanisms of Excitons in Monolayer Transition Metal Dichalcogenides. *Nat. Commun.* **2015**, *6* (1), 8315.
(126) Bertoni, R.; Nicholson, C. W.; Waldecker, L.; Hübener, H.; Monney, C.; De Giovannini, U.; Puppin, M.; Hoesch, M.; Springate, E.; Chapman, R. T. Generation and Evolution of Spin-, Valley-, and Layer-Polarized Excited Carriers in Inversion-Symmetric WSe_2. *Phys. Rev. Lett.* **2016**, *117* (27), 277201.
(127) Beal, A. R.; Knights, J. C.; Liang, W. Y. Transmission Spectra of Some Transition Metal Dichalcogenides. II. Group Via: Trigonal Prismatic Coordination. *J. Phys. C: Solid State Phys.* **1972**, *5* (24), 3540-3551.
(128) Komsa, H.-P.; Krasheninnikov, A. V. Effects of Confinement and Environment on the Electronic Structure and Exciton Binding Energy of MoS_2 from First Principles. *Phys. Rev. B* **2012**, *86* (24), 241201.
(129) Moser, S. An Experimentalist's Guide to the Matrix Element in Angle Resolved Photoemission. *J. Electron. Spectrosc. Relat. Phenom.* **2017**, *214*, 29-52.
(130) He, K. L.; Kumar, N.; Zhao, L.; Wang, Z. F.; Mak, K. F.; Zhao, H.; Shan, J. Tightly Bound Excitons in Monolayer WSe_2. *Phys. Rev. Lett.* **2014**, *113* (2).
(131) Bian, A.; He, D. W.; Hao, S. C.; Fu, Y.; Zhang, L.; He, J. Q.; Wang, Y. S.; Zhao, H. Dynamics of Charge-Transfer Excitons in a Transition Metal Dichalcogenide Heterostructure. *Nanoscale* **2020**, *12* (15), 8485-8492.
(132) Li, M. Y.; Shi, Y. M.; Cheng, C. C.; Lu, L. S.; Lin, Y. C.; Tang, H. L.; Tsai, M. L.; Chu, C. W.; Wei, K. H.; He, J. H.; Chang, W. H.; Suenaga, K.; Li, L. J. Epitaxial Growth of a Monolayer WSe_2-MoS_2 Lateral p-n Junction with an Atomically Sharp Interface. *Science* **2015**, *349* (6247), 524-528.

(133) Kilina, S. V.; Neukirch, A. J.; Habenicht, B. F.; Kilin, D. S.; Prezhdo, O. V. Quantum Zeno Effect Rationalizes the Phonon Bottleneck in Semiconductor Quantum Dots. *Phys. Rev. Lett.* **2013**, *110* (18), 180404.

(134) Craig, C. F.; Duncan, W. R.; Prezhdo, O. V. Trajectory Surface Hopping in the Time-Dependent Kohn-Sham Approach for Electron-Nuclear Dynamics. *Phys. Rev. Lett.* **2005**, *95* (16), 163001.

(135) Grundmann, M.; *The Physics of Semiconductors*, 3rd ed.; Springer-Verlag: Berlin, 2015.

(136) Li, Y.; Cui, Q.; Ceballos, F.; Lane, S. D.; Qi, Z.; Zhao, H. Ultrafast Interlayer Electron Transfer in Incommensurate Transition Metal Dichalcogenide Homobilayers. *Nano Lett.* **2017**, *17* (11), 6661-6666.

(137) He, J.; Kumar, N.; Bellus, M. Z.; Chiu, H.-Y.; He, D.; Wang, Y.; Zhao, H. Electron Transfer and Coupling in Graphene–Tungsten Disulfide Van Der Waals Heterostructures. *Nat. Commun.* **2014**, *5* (1), 5622.

(138) Lo, S.-Z. A.; Wang, L.; Loh, Z.-H. Pulse Propagation in Hollow-Core Fiber at High-Pressure Regime: Application to Compression of Tens of μJ Pulses and Determination of Nonlinear Refractive Index of Xenon at 1.03μm. *Appl. Opt.* **2018**, *57* (16), 4659-4664.

(139) Aeschlimann, M.; Brixner, T.; Fischer, A.; Kramer, C.; Melchior, P.; Pfeiffer, W.; Schneider, C.; Strüber, C.; Tuchscherer, P.; Voronine, D. V. Coherent Two-Dimensional Nanoscopy. *Science* **2011**, *333* (6050), 1723-1726.

(140) Liang, Y.; Li, B.-H.; Li, Z.; Zhang, G.; Sun, J.; Zhou, C.; Tao, Y.; Ye, Y.; Ren, Z.; Yang, X. Spatially Heterogeneous Ultrafast Interfacial Carrier Dynamics of 2D-MoS_2 Flakes. *Mater. Today Phys.* **2021**, *21*, 100506.

(141) Buckanie, N. M.; Göhre, J.; Zhou, P.; von der Linde, D.; Horn-von Hoegen, M.; Meyer zu Heringdorf, F. J. Space Charge Effects in Photoemission Electron Microscopy Using Amplified Femtosecond Laser Pulses. *J. Phys.: Condens. Matter* **2009**, *21* (31), 314003.

(142) Schönhense, B.; Medjanik, K.; Fedchenko, O.; Chernov, S.; Ellguth, M.; Vasilyev, D.; Oelsner, A.; Viefhaus, J.; Kutnyakhov, D.; Wurth, W.; Elmers, H. J.; Schönhense, G. Multidimensional Photoemission Spectroscopy—the Space-Charge Limit. *New J. Phys.* **2018**, *20* (3), 033004.

(143) Kresse, G.; Hafner, J. Ab Initio Molecular Dynamics for Liquid Metals. *Phys. Rev. B* **1993**, *47* (1), 558-561.

(144) Kresse, G.; Furthmüller, J. Efficient Iterative Schemes for Ab Initio Total-Energy Calculations Using a Plane-Wave Basis Set. *Phys. Rev. B* **1996**, *54* (16), 11169-11186.
(145) Ernzerhof, M.; Scuseria, G. E. Assessment of the Perdew–Burke–Ernzerhof Exchange-Correlation Functional. *J. Chem. Phys.* **1999**, *110* (11), 5029-5036.
(146) Kresse, G.; Joubert, D. From Ultrasoft Pseudopotentials to the Projector Augmented-Wave Method. *Phys. Rev. B* **1999**, *59* (3), 1758-1775.
(147) Grimme, S.; Antony, J.; Ehrlich, S.; Krieg, H. A Consistent and Accurate Ab Initio Parametrization of Density Functional Dispersion Correction (DFT-D) for the 94 Elements H-Pu. *J. Chem. Phys.* **2010**, *132* (15), 154104.
(148) Tully, J. C. Molecular Dynamics with Electronic Transitions. *J. Chem. Phys.* **1990**, *93* (2), 1061-1071.
(149) Fischer, S. A.; Habenicht, B. F.; Madrid, A. B.; Duncan, W. R.; Prezhdo, O. V. Regarding the Validity of the Time-Dependent Kohn–Sham Approach for Electron-Nuclear Dynamics Via Trajectory Surface Hopping. *J. Chem. Phys.* **2011**, *134* (2), 024102.
(150) Jaeger, H. M.; Fischer, S.; Prezhdo, O. V. Decoherence-Induced Surface Hopping. *J. Chem. Phys.* **2012**, *137* (22), 22A545.
(151) Akimov, A. V.; Prezhdo, O. V. Persistent Electronic Coherence Despite Rapid Loss of Electron–Nuclear Correlation. *J. Phys. Chem. Lett.* **2013**, *4* (22), 3857-3864.
(152) Silbey, R. J. Principles of Nonlinear Optical Spectroscopy by Shaul Mukamel (University of Rochester). Oxford University Press: New York. 1995. Xviii + 543 Pp. $65.00. Isbn 0-19-509278-3. *J. Am. Chem. Soc.* **1996**, *118* (50), 12872-12872.
(153) Akimov, A. V.; Prezhdo, O. V. The PYXAID Program for Non-Adiabatic Molecular Dynamics in Condensed Matter Systems. *J. Chem. Theory Comput.* **2013**, *9* (11), 4959-4972.
(154) Akimov, A. V.; Prezhdo, O. V. Advanced Capabilities of the PYXAID Program: Integration Schemes, Decoherence Effects, Multiexcitonic States, and Field-Matter Interaction. *J. Chem. Theory Comput.* **2014**, *10* (2), 789-804.
(155) Neukirch, A. J.; Hyeon-Deuk, K.; Prezhdo, O. V. Time-Domain Ab Initio Modeling of Excitation Dynamics in Quantum Dots. *Coord. Chem. Rev.* **2014**, *263*, 161-181.
(156) Chu, W. B.; Saidi, W. A.; Prezhdo, O. V. Long-Lived Hot Electron in a Metallic Particle for Plasmonics and Catalysis: Ab Initio Nonadiabatic Molecular Dynamics with Machine Learning. *ACS Nano* **2020**, *14* (8), 10608-10615.

(157) Sarkar, R.; Kar, M.; Habib, M.; Zhou, G. Q.; Frauenheim, T.; Sarkar, P.; Pal, S.; Prezhdo, O. V. Common Defects Accelerate Charge Separation and Reduce Recombination in Cnt/Molecule Composites: Atomistic Quantum Dynamics. *J. Am. Chem. Soc.* **2021**, *143* (17), 6649-6656.
(158) Li, W.; She, Y. L.; Vasenko, A. S.; Prezhdo, O. V. Ab Initio Nonadiabatic Molecular Dynamics of Charge Carriers in Metal Halide Perovskites. *Nanoscale* **2021**, *13* (23), 10239-10265.
(159) Tomko, J. A.; Runnerstrom, E. L.; Wang, Y. S.; Chu, W. B.; Nolen, J. R.; Olson, D. H.; Kelley, K. P.; Cleri, A.; Nordlander, J.; Caldwell, J. D.; Prezhdo, O. V.; Maria, J. P.; Hopkins, P. E. Long-Lived Modulation of Plasmonic Absorption by Ballistic Thermal Injection. *Nat. Nanotechnol.* **2021**, *16* (1).
(160) Zhang, L. L.; Chu, W. B.; Zhao, C. Y.; Zheng, Q. J.; Prezhdo, O. V.; Zhao, J. Dynamics of Photoexcited Small Polarons in Transition-Metal Oxides. *J. Phys. Chem. Lett.* **2021**, *12* (9), 2191-2198.
(161) Li, H.; Contryman, A. W.; Qian, X.; Ardakani, S. M.; Gong, Y.; Wang, X.; Weisse, J. M.; Lee, C. H.; Zhao, J.; Ajayan, P. M.; Li, J.; Manoharan, H. C.; Zheng, X. Optoelectronic Crystal of Artificial Atoms in Strain-Textured Molybdenum Disulphide. *Nat. Commun.* **2015**, *6* (1), 7381.

Table of contents graphic